Estimating global landslide susceptibility and its uncertainty through ensemble modelling

Anne Felsberg[1], Jean Poesen[1,2], Michel Bechtold[1], Matthias Vanmaercke[1], and Gabriëlle J. M. De Lannoy[1]

[1]KU Leuven, Department of Earth and Environmental Sciences, Belgium
[2]Maria-Curie Sklodowska University, Faculty of Earth Sciences and Spatial Management, Lublin, Poland

Correspondence: Anne Felsberg (anne.felsberg@kuleuven.be)

Abstract. This study assesses global landslide susceptibility (*LSS*) at the coarse 36-km spatial resolution of global satellite soil moisture observations, to prepare for a subsequent combination of a global *LSS* map with dynamic satellite-based soil moisture estimates for landslide modelling. Global *LSS* estimation contains uncertainty, arising from errors in the underlying data, the spatial mismatch between landslide events and predictor information, and large-scale *LSS* model generalizations. For a reliable uncertainty assessment, this study combines methods from the landslide community with common practices in meteorological modelling to create an ensemble of global *LSS* maps. The predictive *LSS* models are obtained from a mixed effects logistic regression, associating hydrologically-triggered landslide data from the Global Landslide Catalog (GLC) with predictor variables describing the landscape. The latter are taken from the Catchment land surface modeling system (incl. input parameters of soil (hydrological) properties and resulting climatological statistics of water budget estimates), geomorphological and lithological data. Road network density is introduced as a random effect to mitigate potential landslide inventory bias. We use a blocked random cross validation to assess the *model uncertainty* that propagates into the *LSS* maps. To account for other uncertainty sources, such as *input uncertainty*, we also perturb the predictor variables and obtain an ensemble of *LSS* maps. The perturbations are optimized so that the *total predicted uncertainty* fits the observed discrepancy between the ensemble average *LSS* and the landslide presence or absence from the GLC. We find that the most reliable *total uncertainty* estimates are obtained through the inclusion of a topography-dependent perturbation between 15% and 20% to the predictor variables. The areas with the largest *LSS* uncertainty coincide with moderate ensemble average *LSS*, because of the asymptotic nature of the *LSS* model. The spatial patterns of the average *LSS* agree well with previous global studies and yield areas under the Receiver Operating Characteristic between 0.84 and 0.92 for independent regional to continental landslide inventories.

1 Introduction

Mitigating landslide impacts requires a good understanding of the spatial and temporal patterns of landslide occurrence. The spatial likelihood of a landslide is referred to as landslide susceptibility (*LSS*) and plays a crucial role in risk assessment and land use planning (Guzzetti et al., 2005; Crozier, 2013; Reichenbach et al., 2018). Regional high-resolution *LSS* maps derived from environmental conditions are a fundamental tool for informing local population, city planners and decision makers both

on the immanent landslide likelihood, but also about secondary effects such as major sediment sources (Crozier, 2013; Maes et al., 2017; Broeckx et al., 2020). Large scale low-resolution *LSS* maps can serve as background information to be downscaled for the above applications at the local scale, or they can be used in conjunction with large-scale satellite data to construct a spatio-temporal estimate of the likelihood for a landslide.

Due to their generalizing nature, *LSS* models are prone to uncertainty (Petschko et al., 2014). A large number of *LSS* models exists, but most focus on local to regional scales and typically lack thorough validation or uncertainty assessment (Reichenbach et al., 2018). Recent advances in computational power and data availability have fostered the development of *LSS* maps at continental level (for example Europe: Wilde et al. (2018) and Van Den Eeckhaut et al. (2012), Africa: Broeckx et al. (2018)) or at the global scale (for example Nadim et al. (2006); Hong et al. (2007); Lin et al. (2017); Stanley and Kirschbaum (2017)). While information about the uncertainty would be essential to know how reliable these large scale *LSS* maps are as well as how much variation can be expected within a mapping unit, only Broeckx et al. (2018) provide such a measure for their map of Africa and only to a limited degree. The quantification of *LSS* uncertainty becomes even more called for yet challenging at the global scale and with coarser spatial resolution due to necessary generalizations and the increased spatial mismatch between landslide events and predictor information. A reliable uncertainty assessment of global *LSS* estimates is moreover crucial when subsequently combining them in a statistically optimal way with, for example, satellite soil moisture products from Soil Moisture Ocean Salinity (SMOS) or Soil Moisture Active Passive (SMAP) as used by Felsberg et al. (2021).

Uncertainty is typically grouped according to its origin into *model uncertainty* (here: 'How correct are the equations that we use to predict *LSS*?') and *input uncertainty* (here: 'How correct is the input to these equations?'). *Model uncertainty* stems from heuristic choices that are necessary in the process of model creation, including the choice of the statistical modelling approach, the selection of predictor variables, training data sampling and training data quality (see for example Steger et al. (2015); Pourghasemi and Rossi (2016); Zêzere et al. (2017); Depicker et al. (2020); Lima et al. (2021)). In order to estimate some of these model-intrinsic errors for a chosen modelling approach, cross validation (CV) is a widely used method where data is divided into a number of subsets, that are subsequently used for training and testing of the model. How to best sample the CV subsets to retrieve realistic uncertainty estimates is in itself a field of research. For *LSS* maps, random sampling is most common (see for example Broeckx et al. (2018)), while spatial sampling is used less often for an additional uncertainty estimate (see for example Steger et al. (2020) or Depicker et al. (2020)). However, these are known to respectively strongly under- and possibly overestimate the *model uncertainty*, and hybrid methods such as blocked random CV (B-CV) have been suggested to result in the most reliable uncertainty estimates (Roberts et al., 2017). CV leads to multiple *LSS* model equations (one per CV subset) and the standard deviation of the resulting *LSS* values gives an indication of the associated *model uncertainty* as shown by Broeckx et al. (2018) for Africa.

Input uncertainty principally results from errors in the environmental data. To assess how *input uncertainty* propagates into the *total prediction uncertainty*, ensemble simulations can be used. Meteorologists, for example, simulate the weather based on a distribution of initial conditions and predict an ensemble of equally possible outcomes (ensemble members). Instead of only one deterministic weather forecast, they use the ensemble average prediction that has been found to perform better than their

deterministic counterpart (Kalnay et al., 2006). The uncertainty of the final ensemble average prediction can then be estimated by the variance or standard deviation among the ensemble members.

60   The *total ensemble uncertainty*, resulting from the combination of these methods that account for *model* and *input uncertainty* respectively, is assumed to be reliable if it matches the observed 'actual' *total uncertainty*. The latter is estimated by comparing the predicted average *LSS* against the observed presence and absence of landslides. The gap between this observed and the predicted *total uncertainty* can then be closed by tuning the magnitude of the ensemble input perturbations. Note that this implies that the perturbations might in the end not purely capture the *input uncertainty*, but actually compensate for other

65   sources of uncertainty as well that are not specifically addressed. One such important source of uncertainty is spatial representativeness error (Blöschl and Sivapalan, 1995; van Leeuwen, 2015), especially when evaluating spatially averaged grid cell *LSS* estimates using single landslide observations as reference data.

In this study, we combine CV and an ensemble approach to create global *LSS* maps with a reliable *total uncertainty* (full ensemble standard deviation). We create multiple *LSS* equations as part of CV ('weak model constraint'), and subsequently

70   perturb the selected predictor variables (input of the *LSS* model equations) to retrieve a 'full ensemble' of possible *LSS* values. Specifically, we focus on hydrologically-triggered landslides and propose to include long-term climatological statistics of hydrometeorological variables as predictor variables, in addition to the common geomorphological ones. We use a mixed effects logistic regression (MELR) relying on the strong generalizing capabilities of logistic regression as the basic model structure, and we mitigate the potential reporting bias of landslide *presences* in the Global Landslide Catalog (GLC) with stratified aver-

75   age road network density (RND) as a random effect. To limit biases from unreliable and confounding definitions of landslide *absence* grid cells for the model creation, we introduce a novel approach based on a 'characteristic distance' between landslides. After having taken these steps to limit the introduced uncertainty, the B-CV is used to instill *model uncertainty* via a selection of different possible predictor variables and associated parameters, and we further add (and tune) ensemble perturbations to the selected predictor variables to obtain a reliable *total ensemble uncertainty*. This *LSS* assessment is carried out on the

80   36-km Equal-Area Scalable Earth version 2 (EASEv2) grid, in line with the nominal spatial resolution of satellite soil moisture estimates from SMOS or SMAP. Producing spatial *LSS* estimates at this resolution facilitates a subsequent combination with the satellite-based temporally dynamic data, as well as calculations of the above mentioned climatological statistics and the development of computationally intense ensemble approaches. To our knowledge, no framework has earlier been developed for the assessment of the *total uncertainty* of *LSS* predictions.

85   Section 2 introduces the landslide (presence, absence) and environmental data used to create ensemble *LSS* maps. The *LSS* model construction based on MELR is introduced in Sect. 3, along with the methods of CV and input predictor variable perturbations for uncertainty assessment, and methods to evaluate the results. Section 4 presents the resulting *LSS* model structure and selected predictor variables, and the ensemble *LSS* evaluation for different input perturbations. Section 5 discusses various aspects of the results. The paper closes with a summarizing conclusion.

2 Data

2.1 Landslide data

A first step in creating our *LSS* models is the creation of suitable training datasets, indicated in the upper part of the flowchart in Fig. 1. We use reported hydrologically-triggered landslide occurrences from the most recent version of the GLC (https://-landslides.nasa.gov/viewer, accessed 8th February 2021). The GLC is a landslide inventory that contains information about location, date and trigger. It is originally based on media reports (Kirschbaum et al., 2010, 2015) but has recently been supplemented with the citizen science-based Landslide Reporter Catalog (LRC) data (Juang et al., 2019), see Stanley et al. (2021) for details. Any reference to the GLC hereafter refers to this combined data product. Despite known English-language and economic biases (Kirschbaum et al., 2010, 2015), the GLC covers all continents and landslide hotspots. It has already been used for the creation of two global *LSS* maps (Stanley and Kirschbaum, 2017; Lin et al., 2017) and was used to train the newest version of the Landslide Hazard Assessment for Situational Awareness (LHASA) model version 2.0 (Stanley et al., 2021).

For this study, we use 12515 hydrologically-triggered landslides (GLC classifiers "continuous rain", "downpour", "monsoon", "flooding", "rain" and "tropical cyclone") reported mainly between January 2007 and November 2020. Since *LSS* informs about the static environmental landslide likelihood, it is common practice to exclude the temporal aspect of landslide occurrence and instead work with landslide presence and absence locations. Multiple landslides within the same 36-km EASEv2 grid cell are therefore aggregated into one 'landslide presence grid cell', resulting in a total of $N_{LS}=3757$ (orange grid cells, Fig. A1). While we acknowledge that grid cells with more frequent landslide reporting can in general be expected to have a higher *LSS*, we found that the information about the frequency of landslide occurrence within a grid cell strongly mirrors biases in the landslide inventory, e.g. more landslides are reported in English-speaking countries. The aggregation, on the contrary, reduces the landslide presence reporting bias of the GLC. To address the remaining landslide presence bias originating from more landslide reporting in frequently accessed areas, we use stratified data on the RND (including highways and all types of roads, ranging from primary to local roads) provided by the Global Roads Inventory Project (GRIP) (Meijer et al., 2018) as a random effect, explained in Sect. 3.1.

The creation of realistic statistical *LSS* models and uncertainty estimates depends on the knowledge of both landslide presences and absences (Roberts et al., 2017; Steger and Glade, 2017; Knevels et al., 2020; Lucchese et al., 2021). Usually, an absence grid cell is simply defined as one without a recorded landslide. For local modelling, this might work when complete and reliable landslide inventories are available. For large or remote areas, however, no reported landslide does not necessarily mean that the site never experienced one. Terrain features show a certain amount of spatial autocorrelation indicating that locations in proximity of a known landslide are generally prone to instability as well. It should therefore be avoided to use grid cells too close to known landslide locations as an absence reference (Brenning, 2005). On the other hand, absence grid cells sampled very far from the reported landslide locations, in so-called 'trivial' or easily classifiable areas (for example flat areas), might result in an underrepresentation of stable areas in the vicinity of the known landslide locations (Steger and Glade, 2017). Additionally, it might confound the selection process of geomorphologically meaningful predictor variables and lead to an overoptimistic conception of the resulting *LSS* map's quality (Steger and Glade, 2017; Lucchese et al., 2021).
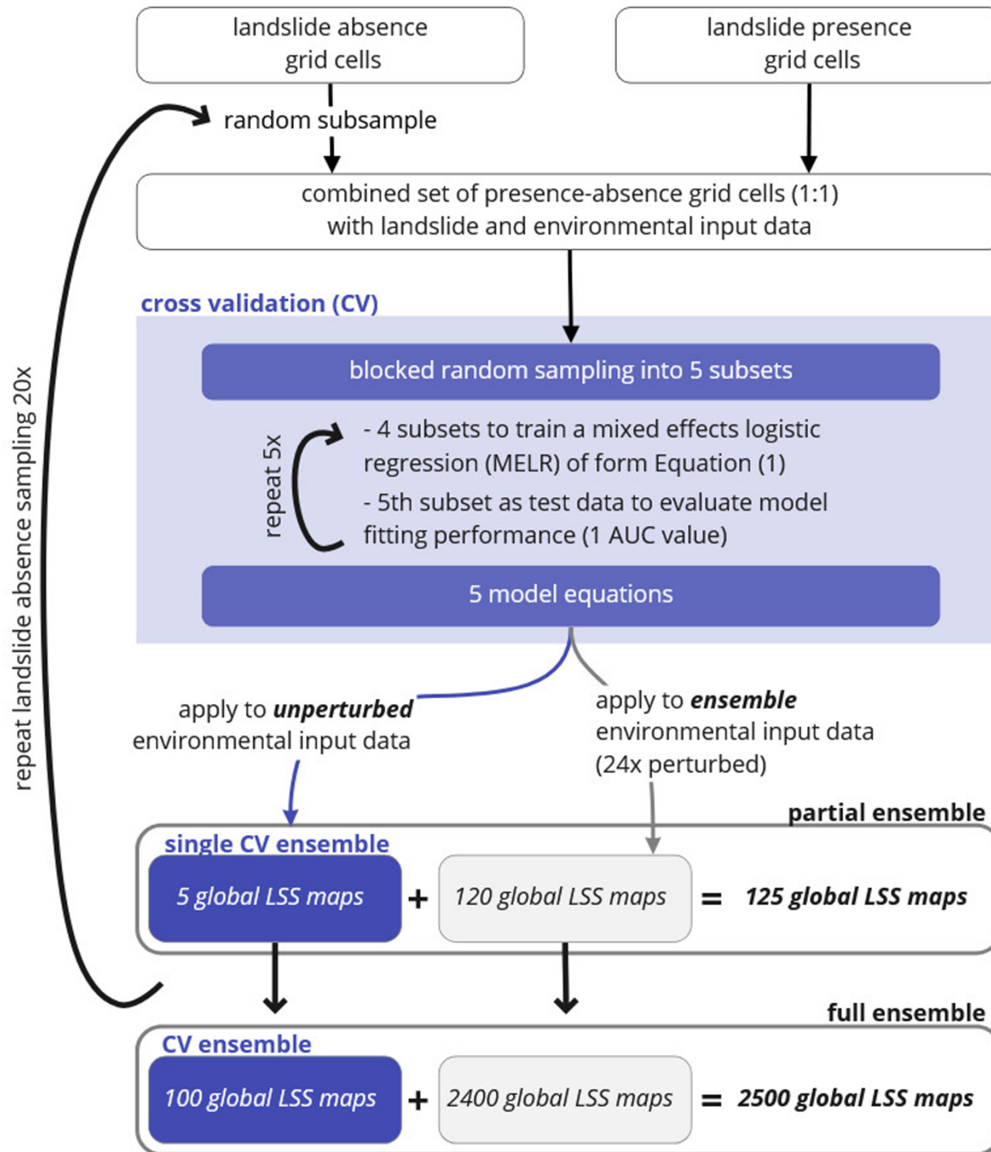
Figure 1. Schematic of methodology used in this study to derive ensembles of global landslide susceptibility (*LSS*) maps. 'Ensemble' refers to a collection of *LSS* maps. In the course of this study, we refer to different subsets of the **full ensemble** (LSS_{2500}), namely the ensemble from one single blocked random CV application (**single CV ensemble**, LSS_5), when adding input perturbations to it (**partial ensemble**, LSS_{125}) or when repeating the underlying landslide absence subsampling (**CV ensemble**, LSS_{100}). Subscript numbers indicate the size of the *LSS* ensemble. Model fitting performance is evaluated during the process of cross validation (CV) by calculating the area under the Receiver Operating Characteristic curve (AUC) for each model equation of form Equation 1.

In this study, we therefore adopt a sampling strategy as used in earlier *LSS* assessments (Van Den Eeckhaut et al., 2012; Lin et al., 2017; Zhu et al., 2017; Nowicki Jessee et al., 2018; Knevels et al., 2020; Lucchese et al., 2021), where reliable absence grid cells are defined between a minimum (buffer) and maximum radius around known landslide presence grid cells. As a measure of spatial autocorrelation we derive the 'characteristic distance' between two landslides from the GLC (for details see Appendix A1). We use this characteristic distance of 221.43 km (~ 6 grid cells) as the buffer radius, and 2.5 times this distance (~ 15 grid cells) as maximum radius. Absence grid cells are hence selected from grid cells 7 to 15 around a landslide occurrence (blue grid cells in Fig. A1). This definition still results in more than six times more absence grid cells ($N_{noLS} > 25000$) than landslide presence grid cells ($N_{LS}=3757$). We therefore randomly sample from the absence grid cells with a 1:1 ratio ($N_{LS}:N_{noLS}$) as is commonly done, for example by Brenning (2005), Steger and Glade (2017), Nowicki Jessee et al. (2018), Depicker et al. (2020), Knevels et al. (2020), Lin et al. (2021) and Lucchese et al. (2021). *LSS* models are subsequently constructed based on data from 7514 (absence + presence) grid cells, as illustrated in Fig. 1.

2.2 Environmental data

The 77 predictor variables considered in this study are listed in Table 1 and were selected based on earlier reviews on the most common predictors used for *LSS* maps (Pourghasemi and Rossi, 2016; Reichenbach et al., 2018). In statistical *LSS* models, these predictor variables act as proxies for one or multiple processes underlying a landslide (Whiteley et al., 2019). Since *LSS* is referring to the spatial likelihood of landslides, we only consider predictor variables that are (quasi) static in time.

To better represent processes underlying hydrologically-triggered landslides, we include long-term climatological statistics of soil moisture in different layers, soil surface temperature, runoff, rainfall, evaporation and snow depth as possible predictor variables. These climatological statistics include the range (here defined as the difference between percentiles 1 and 99), inter-quartile range, mean, median, percentile 99 and maximum within the time period 1990-2020, derived from 36-km simulations with the Catchment Land Surface Model (CLSM) (Koster et al., 2000; Reichle et al., 2019), forced with Modern-Era Retrospective analysis for Research and Applications, Version 2 (MERRA-2) meteorological data, as in Felsberg et al. (2021).

Most other predictor variables are part of the 36-km input parameters to the CLSM. Of these, elevation and compound topographic index (CTI) stem from the same underlying Shuttle Radar Topography Mission (SRTM) data as the morphological information on slope from the United States Geological Survey (USGS), but with different data sources for the high northern latitudes (Verdin et al., 2007).

We use lithological information from the Global Lithological Map (GLiM) (Hartmann and Moosdorf, 2012) aggregated to the fraction of a grid cell covered by each of the 13 lithological classes (we exclude the classes 'water', 'ice and glacier', and 'no data'). This produces a dataset with 13 fields, each with a continuous fraction estimate. Peak ground acceleration (PGA) is the likely level of ground motion from earthquakes (Giardini et al., 2003). Here, we do not use it as the likelihood of a seismic landslide trigger, but rather as a proxy for the fracturation and weakening that lithologies have undergone due to seismic and tectonic activity (Lin et al., 2017; Vanmaercke et al., 2017; Broeckx et al., 2018). Details on the aggregation methods are given in Table 1.

Table 1. Environmental predictor variables used in this study, alongside their data source, original spatial resolution and methods used for aggregation to the 36 km EASEv2 grid. Apart from slope, lithology, PGA and rainfall, the specified aggregation was not conducted in this study. Predictor variables that are part of the CLSM parameter set or output do not require any spatial aggregation. Long-term climatological statistics of all hydrological variables comprise the range (here: difference between 1st and 99th percentile), inter-quartile range, mean, median, 99th percentile and maximum between 1990 and 2020. MERRA-2 precipitation is used as input for the calculations of the hydrological climatological statistics and has been interpolated to the 36 km EASEv2 grid as part of the simulation process. Units are given for the original data, but are removed through the rescaling of the data to the interval (0,1) (see text).

Predictor variables	Data source	Original spatial resolution	Aggregation method to or within EASEv2, 36 km grid cell
slope (mean, maximum) [°]	USGS: details in Verdin et al. (2007) based on SRTM DEM[a] and GTOPO30[b]	3" (SRTM DEM), 30" (GTOPO30)	mean and maximum
elevation (mean, standard deviation) [m a. s. l.]	CLSM parameters: details in Verdin (2013) based on SRTM DEM[a] and GMTED2010[c]	3" (SRTM DEM), 7.5" (GMTED2010)	mean and standard deviation
depth to bedrock [m]	CLSM parameters: details in De Lannoy et al. (2014) based on GSWP-2[d]	1°	spatial interpolation
percentage of gravel (0-30 cm) [vol%]	CLSM parameters details in De Lannoy et al. (2014) based on STATSGO2[e] and HWSD1.21[f]	30"	most representative 30" sample
percentage of clay (0-30 cm and 0-100 cm) [w%]			
percentage of sand (0-30 cm and 0-100 cm) [w%]			
porosity (0-30 cm and 0-100 cm) [m³/m³]			
wilting point divided by porosity (0-30 cm and 0-100 cm) [-]			
compound topographic index, CTI (mean, maximum) = ln(specific catchment area/tan(slope)) [log(m)]	CLSM parameters: details in Verdin (2013) based on SRTM DEM[a] and GMTED2010[c]	3" (SRTM DEM), 7.5" (GMTED2010)	mean and maximum
land fraction within grid cell	CLSM parameters: HYDRO1k based on GTOPO30, 1996 (EROS, 2018; Verdin, 2013)	10"	areal fraction
fraction covered by each of 13 lithological classes [-]: *metamorphic rocks, mixed sedimentary rocks, siliclastic sedimentary rocks, basic plutonic rocks, acid plutonic rocks, basic volcanic rocks, intermediate volcanic rocks, carbonate sedimentary rocks, unconsolidated sediments, intermediate plutonic rocks, pyroclastics, evaporites, acid volcanic rocks*	GLiM created by Hartmann and Moosdorf (2012)	polygons	areal fraction
peak ground acceleration, PGA [m/s²] due to earthquakes expected with a return period of 475 years (i.e. 10% exceedance probability in 50 years)	GSHM[g] created by GSHAP[h] (Giardini et al., 2003)	1°	nearest neighbour
rainfall climatological statistics [mm]	MERRA-2 (Bosilovich, 2015)	0.625° lon x 0.5° lat	bilinear interpolation
surface soil moisture climatological statistics (0-5 cm) [m³/m³]	CLSM output	EASEv2, 36 km	-
root zone soil moisture climatological statistics (0-100 cm) [m³/m³]			
profile soil moisture climatological statistics (0-100 cm) [m³/m³]			
land surface temperature climatological statistics [K]			
runoff climatological statistics [mm]			
evaporation (incl. transpiration) climatological statistics [mm]			
snow depth climatological statistics [mm]			

[a] Shuttle Radar Topography Mission digital elevation model; [b] USGS global elevation model; [c] Global Multi-resolution Terrain Elevation Data 2010; [d] Second Global Soil Wetness Project; [e] State Soil Geographic project; [f] Harmonized World Soil Databank version 1.21; [g] Global Seismic Hazard Map; [h] Global Seismic Hazard Assessment Project;

3 Model construction and evaluation

This section introduces the methods used in this study for model construction and evaluation. Section 3.1 introduces the general principles of logistic regression used to derive global *LSS* estimates, before elaborating the predictor variable selection process and the implementation of average road network density as a random effect. Section 3.2 introduces methods for uncertainty assessment. First, cross validation is introduced with a detailed explanation of the blocked random sampling. Second, the methods of input ensemble perturbations are briefly explained (details are elaborated in Appendix A2). *LSS* results based on the first approach alone are referred to as 'CV ensemble' or LSS_{100}. Results based on both CV and input ensemble perturbations are referred to as 'full ensemble' or LSS_{2500}. Section 3.3 introduces the methods and data used for the evaluation of ensemble average *LSS* and the impact of the extended uncertainty assessment through input perturbations.

3.1 Mixed effects logistic regression (MELR) for model development

In this study, we create a statistical *LSS* model using MELR (Zuur, 2009), as previously also employed by Steger et al. (2017), Lin et al. (2021) and Lima et al. (2021). Logistic regression is the most commonly used approach for statistical *LSS* mapping (Reichenbach et al., 2018). It is associated with strong generalizing capabilities (Brenning, 2005), which is a necessity when working at the global scale, and it has proven to be reliable in continental to global *LSS* assessments (Broeckx et al., 2018; Lin et al., 2017). Within logistic regression, the *LSS*, here defined as the probability of a landslide presence within a grid cell, $P(Y = 1)$, is given by:

$$P(Y = 1) = \frac{exp(\alpha + \sum_{i=1}^{n} \beta_i x_i)}{1 + exp(\alpha + \sum_{i=1}^{n} \beta_i x_i)} \tag{1}$$

with α [-] the intercept, x_i [-] the independent predictor variables, β_i [-] the associated coefficient and n the number of predictor variables. A one unit change in the predictor variable x_i results in a multiplicative change by $exp(\beta_i)$ in the odds of landslide presence, defined as the ratio of $P(Y = 1)/(1 - P(Y = 1)) = exp(\alpha + \sum_{i=1}^{n} \beta_i x_i)$. An increase in the odds of landslide presence is associated with a (non-linear) increase in *LSS*. Positive (negative) β-values hence indicate an increase (decrease) in *LSS* with an increase in the predictor variable. In this study, we work with rescaled predictor variables (between their global minimum and maximum) to detach the magnitude of the β-values from the magnitude of the predictor variable. This facilitates subsequent interpretation.

We employ a stepwise forward technique to select five predictor variables, corresponding to the commonly used number of predictor variables for *LSS* assessment at the global scale (Nadim et al., 2006; Stanley and Kirschbaum, 2017; Lin et al., 2017; Reichenbach et al., 2018). Based on the Akaike information criterion (AIC), a measure that is proportional to the sum of squared errors and allows for comparison between non-nested models, we determine the best performing univariate MELR, i.e. the first predictor variable. The AIC comparison is subsequently repeated for multivariate MELR with one additional predictor variable at a time. This stepwise forward selection also allows to exclude correlated predictor variables ($r > 0.7$, following for example Dormann et al. (2013)), so that largely independent predictor variables are used in the logistic regression. An analysis

of the generated models using the Variance Inflation Factor (VIF) proved that this approach indeed successfully prevented a logistic regression model construction based on predictor variables that are too strongly correlated.

The mixed effects approach allows us to include a categorically scaled variable as a so-called 'random effect', here the random intercept α, for which we use the average road network density (RND) stratified into 6 classes. We summarize all land grid cells where average RND is negligible ($< 1\,m/km^2$) into the first class and use quantiles 20, 40, 60 and 80 of those grid cells with non-negligible RND to divide the rest into additional 5 classes. The mixed effects approach will then result in one global logistic regression equation that has the same β-factors for all grid cells, but 6 different α-values according to each grid cell's RND class. For model fitting purposes it is assumed that these 6 α-values come from a normal distribution (Zuur, 2009).

The underlying assumption of RND as a random effect is that the representativeness of the landslide data from the GLC varies with the RND of the region. We recognize that RND may also serve as a proxy for human interference or likelihood of slope cutting and may hence be included as a predictor variable, as was argued by Stanley and Kirschbaum (2017). The use of RND as a predictor variable or random effect can be expected to have similar results were the connected bias small. For large biases, however, predictions using RND as a predictor variable would systematically underestimate the actual *LSS* of remote areas with strong underreporting of landslides (as was put forward by Steger et al. (2017) for forested areas). The inclusion of RND as a random effect favours the selection of natural, physically valid predictor variables while allowing for locations without roads to also receive a high predicted *LSS*. The inclusion of random effects in a regression model results in unbiased model parameter estimates, but it does not inform about the uncertainty of the predictions (Roberts et al., 2017). We use the glmer function from the lme4 package (Bates et al., 2015) to create MELR models in R version 4.0.3 (R Core Team, 2020) where the best fitting parameters are obtained by maximum likelihood estimation.

3.2 Cross validation (CV) and input perturbations for reliable uncertainty estimation

In this study, the predicted *total ensemble uncertainty* results from the combination of CV techniques and input ensemble perturbations. For CV, the data is separated into 5 subsets, which subsequently are used for training and testing the model with the hold-one-out technique, as illustrated in Fig. 1. We employ a blocked random CV (B-CV), as recommended by Roberts et al. (2017), which we found to indeed yield most realistic error estimates in comparison to random or spatial sampling (not shown). This means that instead of randomly sampling individual grid cells into the 5 subsets for training and testing the model as part of CV, we randomly sample small groups of grid cells with similar environmental conditions, so-called 'blocks' (see Fig. 1). We expect that the environmental conditions are similar in neighbouring pixels (for example same subcontinent) and for similar climate zones. We therefore derive blocks in 2 steps. First, the 7514 grid cells selected for model creation are divided according to 10 predefined (sub-) continents. Within each (sub-) continent, we then derive in a second step 10 blocks through kmeans clustering (Lloyd, 1982) of 30-year average soil surface temperature and rainfall (see Table 1). In total we retrieve 100 blocks comprising different numbers of grid cells (median: 55) that are not necessarily located next to each other. The 100 blocks are then randomly divided into the 5 subsets for model creation (20 each).

Next, the MELR is iteratively trained on 4 subsets and the model fitting performance is tested against the 5th, i.e. the hold-one-out subset, using each subset as a test-subset once (see Fig. 1). This results in 5 different model equations of form

Equation 1 and corresponding *LSS* maps. By repeating the random absence grid cell sub-sampling 20 times, we obtain a total of 100 *LSS* maps (referred to as CV ensemble or LSS_{100}, see Fig. 1) that allow for calculations of an ensemble average *LSS* ($\overline{LSS}_{100}$), as well as a standard deviation ($\sigma_{LSS_{100}}$) per grid cell. Note that the definition of the individual blocks varies between each repetition of absence grid cell sampling due to the kmeans clustering algorithm.

For the input ensemble perturbations, we apply one fitted model equation to a slightly perturbed set of its predictor variable values. In total, 24 repetitions of this process are conducted, resulting in a total ensemble of 25 *LSS* maps per model equation (see Fig. 1). In combination with the 5 model equations and 20 repetitions for the CV ensemble, this results in a total amount of 2500 *LSS* maps (referred to as full ensemble or LSS_{2500}) with corresponding average ($\overline{LSS}_{2500}$) and standard deviation ($\sigma_{LSS_{2500}}$) per grid cell. The latter is representative of the *total prediction uncertainty*.

The aim is to design an *LSS* model setup so that the predicted *total ensemble uncertainty*, quantified by the ensemble variance or spread σ^2_{LSS} matches the discrepancy between predictions and observations which we refer to as the 'actual' uncertainty. A measure of this actual uncertainty is the Brier Score (BS) (Wilks, 2011) which compares the predicted average *LSS* ($\overline{LSS}$) against landslide observations from the GLC (o) at different grid cells i ($i = 1, ..., N$):

$$\text{BS} = \frac{1}{N} \sum_{i=1}^{N} (\overline{LSS} - o)_i^2 \qquad (2)$$

with o being 1 for landslide presence and 0 for absence grid cells. This actual uncertainty by design includes model and input error ($\overline{LSS}$), but also error in the reference data (o), and spatial representativeness error. The perturbations to the predictor variables are randomly sampled from a normal distribution with the mean being the original value of the grid cell. The standard deviation, or perturbation magnitude, is tuned, so that the resulting total ensemble spread (including the spread originating from CV) matches the observed actual uncertainty BS in Equation 2. For details of the tuning process, see Appendix A2. We apply the same perturbation magnitude to all (rescaled) predictor variables. The magnitude is chosen to increase proportionally to the topographic complexity of a location from 15% to 20%. We use the variation of elevation within a grid cell as a measure of said topographic complexity and find this perturbation scaling to yield better results than a globally constant perturbation magnitude. Note that these perturbations in x_i do not linearly propagate into the *LSS* estimates, because the logistic regression (see Equation 1) relates x_i to *LSS* via an S-shape *LSS* curve, with quasi-linear behaviour at the center (i.e. intermediate x_i values) and asymptotic behaviour towards the upper or lower limit (i.e. for very low or high x_i values). Locations of largest perturbation do thus not necessarily coincide with large resulting ensemble uncertainty.

3.3 Evaluation

To quantify how well a predicted *LSS* map represents observed landslide presences and absences, a BS can be used (see Equation 2). Alternatively, the Receiver Operating Characteristic (ROC) is commonly used as evaluation tool for categorical response values such as landslide presence and absence (Reichenbach et al., 2018). For the ROC, the true positive rate of one *LSS* map is displayed against its false positive rate for different possible thresholds in the continuous probability (here: *LSS*) that is predicted. The true positive rate is the proportion of correctly predicted landslide presence grid cells when applying said

threshold ('true positives') of all observed landslide presence grid cells (Wilks, 2011). The false positive rate is the proportion of erroneously predicted landslide presence grid cells ('false positives') of all observed landslide absence grid cells. The area under the ROC curve (AUC) is 1 for a perfect representation of the spatial *LSS* distribution, whereas an AUC value of 0.5 indicates that the model does not perform better than a uniform distribution.

Depending on the reference landslide data, the ROC analysis can be conducted for specific grid cells from a CV subset (independent data not used in the training), or from other independent landslide inventories. Here, we use landslide presence and absence information from the grid cells of the fifth CV subset to assess the model *fitting* performance for each *LSS* ensemble member map 'on the go'. To evaluate the final *prediction* performance of the complete ensemble averages and the corresponding ensemble members, we use 3 independent landslide inventories. We obtain 36-km landslide presence grid cells as described for the GLC in Sect. 2.1 for i) quarterly reports issued by the Russian Federation (FSBIH, 2018) with $N_{LS} = 56$ aggregated from 183 observations, ii) an inventory for Africa by Broeckx et al. (2018) with $N_{LS} = 649$ aggregated from 18053 observations and iii) FraneItalia, a catalog of recent landslides in Italy (Calvello and Pecoraro, 2020) with $N_{LS} = 309$ aggregated from 5438 observations. Since we trust their landslide absence reporting to be reliable, we use all other grid cells within the region in question as landslide absence grid cells. These validation inventories cover different climatic zones and hence landslide regimes, stem from (mostly) non-English speaking regions (Africa, Russia, Italy) and include less populated areas (Africa, Russia), not well represented in the GLC data that underlie our *LSS* estimates. With Italy being a hot-spot of landslide occurrence within Europe, we are moreover able to assess whether the coarse spatial resolution hinders realistic regional assessment within smaller, potentially very susceptible areas.

The AUC and BS metrics can be computed for individual ensemble members (of the CV ensemble LSS_{100}, or the full ensemble LSS_{2500}, yielding a distribution of metrics) or for ensemble averages ($\overline{LSS}_{100}$ and $\overline{LSS}_{2500}$). It will be assessed whether i) an ensemble average outperforms an individual member *LSS* realization, and whether ii) the full ensemble average with ensemble input perturbations ($\overline{LSS}_{2500}$) outperforms the CV ensemble average which does not include input perturbations ($\overline{LSS}_{100}$). This would be in line with the expectations for hydrological or meteorological models (Kalnay et al., 2006).

4 Results

4.1 *LSS* model structure

This section investigates the different values for the β-coefficients and intercept α of the 100 MELR models created following Fig. 1. The landslide absence data, used to train these models, differ for each of the 20 repetitions and subsequently the definitions of the subsets for B-CV vary as well. All 100 models result in *LSS* maps with very high AUC values above 0.8, with a median of 0.92, for the corresponding test data.

The values of the intercept α take negative values for low RND and positive values for high RND (by design, not shown). Figure 2 left panel shows which predictor variables were selected how often and during which step of the selection process (AIC, see Sect. 3.1). The right panel shows boxplots of the β-values for each predictor variable (see Equation 1). Whiskers extend from minimum to maximum and boxes from 25th to 75th quantile, with the median indicated in between. The first
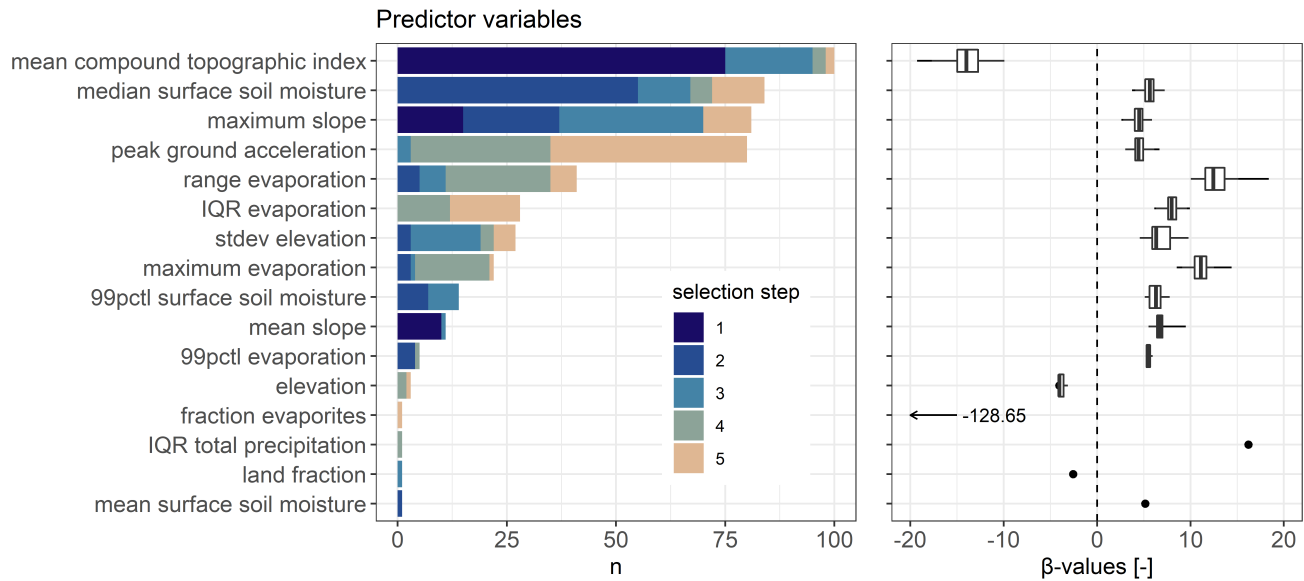
Figure 2. (Left) Frequency of selected predictor variables and (Right) corresponding β-values. The 5 best predictor variables (out of 77, see Table 1) are determined using stepwise forward selection for each MELR model equation (n=100). Colours indicate at which selection step (1-5) the predictor variable was selected. Boxplots for β-values are based on the n values of the left panel, independent of the selection step. Whiskers extend from minimum to maximum β-values. Where $n = 1$, boxplots are replaced by a point.

selected predictor variable was always related to the slope, i.e. either the mean CTI within the grid cell, the maximum slope or the mean slope. The mean CTI, also known as a topographic wetness index, was selected as part of all 100 models. It is inversely proportional to slope (see Table 1), which is in line with the negative β-values, i.e. decrease in *LSS* is expected with

290 increasing CTI. The second selected predictor variable is either another slope measure (maximum slope or standard deviation of the elevation i.e. local relief) or, for more than 65% of the models, related to the climatologic conditions (median surface soil moisture, range of evaporation, maximum evaporation or surface soil moisture). Out of these variables, median surface soil moisture stands out as most frequently being the second predictor variable (for more than 50% of the models). Independent of the selection step, it is part of more than 80% of the models. All of these variables are modeled with positive β-values, i.e. the

295 higher the predictor variable, the larger the odds of a landslide presence and hence the *LSS*.

The areal fraction of evaporites within the grid cell is the only lithological class that was selected, and only in the final selection step. The very unrealistic β-value associated with this predictor (-128.65) suggests that this selection is possibly a statistical artefact. The PGA, treated as a proxy for lithologic weakening due to regular seismic activity, is dominantly selected in the later variable selection steps, but still part of about 80% of the models.
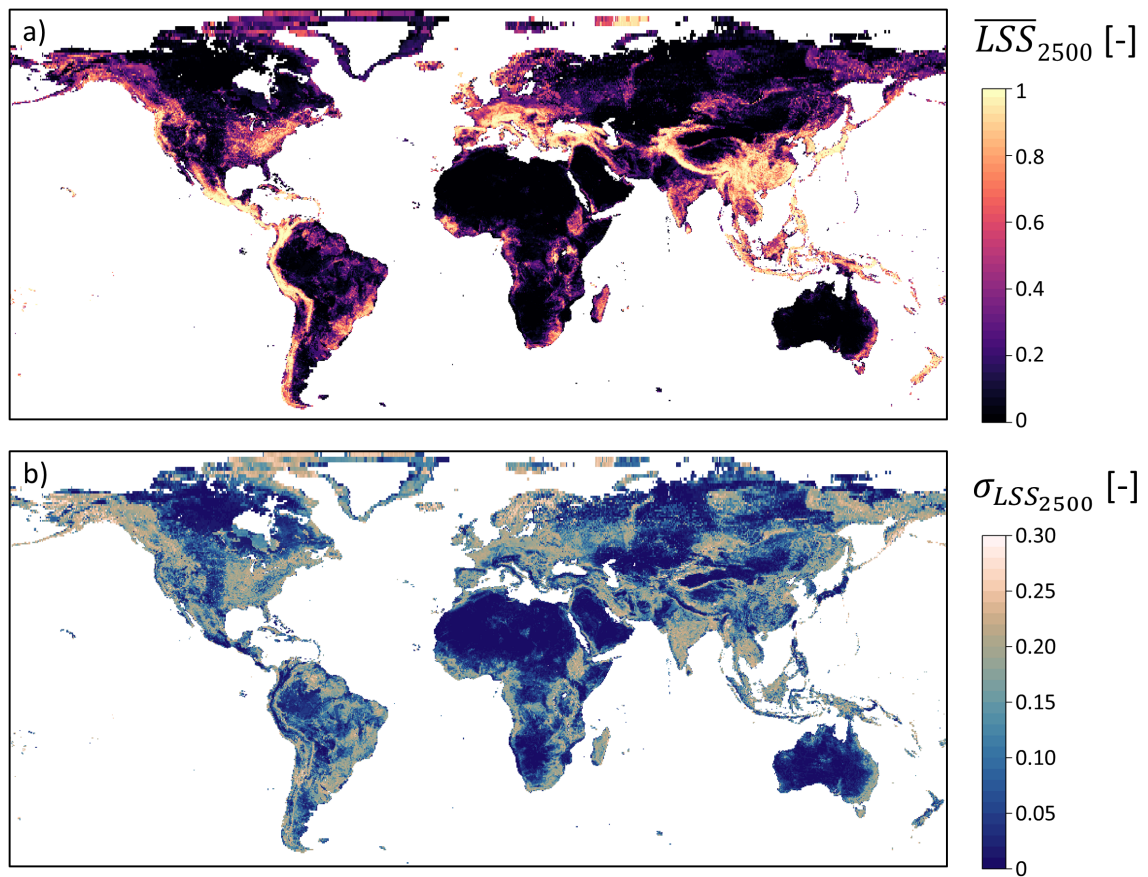
Figure 3. a) Ensemble average *LSS* ($\overline{LSS}_{2500}$) and b) standard deviation ($\sigma_{LSS_{2500}}$) at 36-km resolution. White areas denote missing values (water bodies, ice). Seemingly larger grid cells in the North are characteristic of the EASEv2 grid projection.

4.2 Evaluation of ensemble *LSS*

Based on these 100 model equations, and when perturbing the input parameters (see Fig. 1), we obtain the full ensemble average *LSS* ($\overline{LSS}_{2500}$) and standard deviation ($\sigma_{LSS_{2500}}$) shown in Fig. 3. The highest $\overline{LSS}_{2500}$ can be found in the large mountain ranges on all continents as well as coastal areas (especially the islands in South-East Asia). Very flat areas or planes, such as central northern Canada, Siberia, the Tibetan plateau, the Arabian peninsula, large parts of Africa (especially the Sahara) as well as central Australia have very low $\overline{LSS}_{2500}$. Intermediate $\overline{LSS}_{2500}$ values are found in the northern Rocky Mountains towards Alaska as well as the Kolyma Range in Russia, at the north-eastern shores of South America and the western shores of Africa, along the East African Rift, Scandinavia and India. Figure 4a shows a density scatter plot of $\sigma_{LSS_{2500}}$ versus $\overline{LSS}_{2500}$.
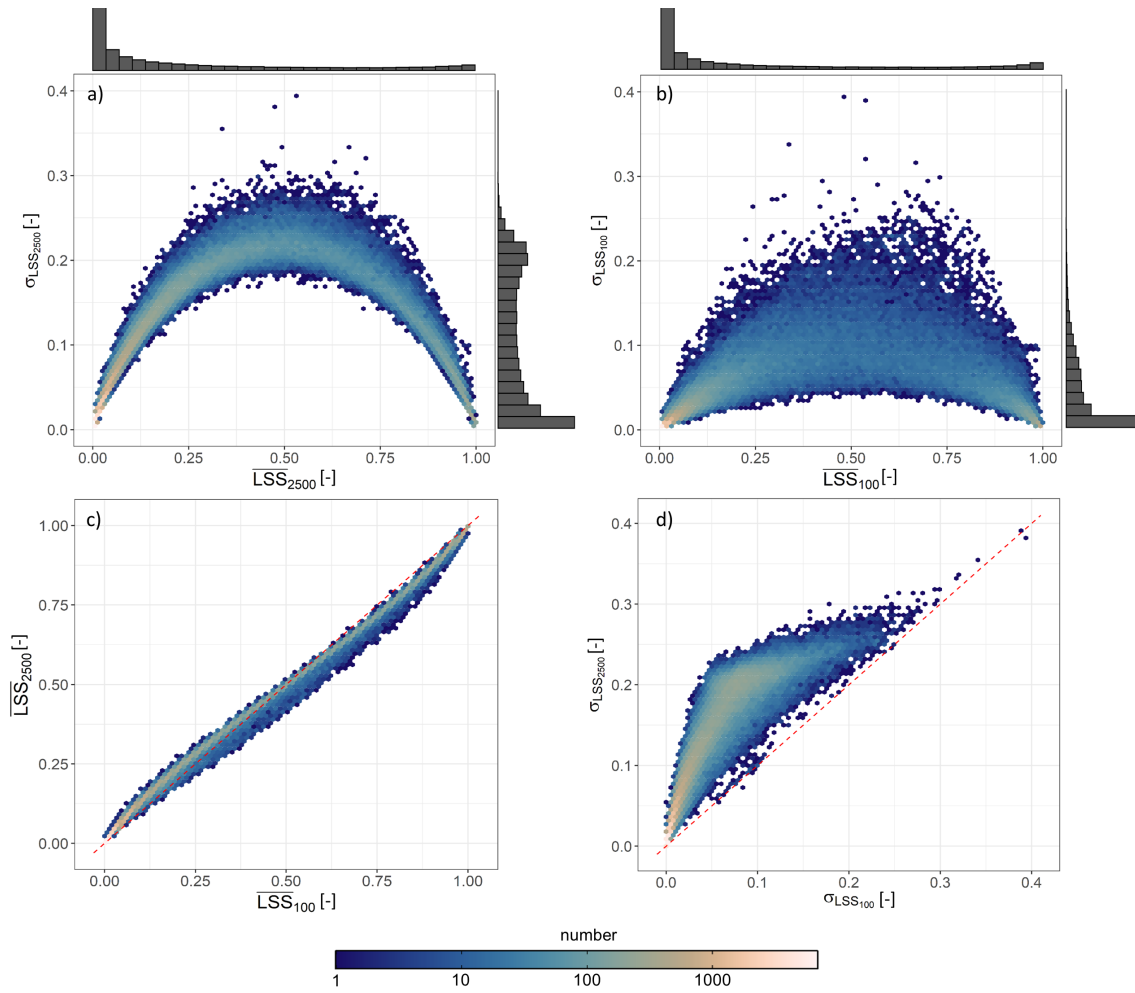
Figure 4. (Top) Ensemble standard deviation LSS (σ_{LSS}) versus ensemble average ($\overline{LSS}$) of a) the full ensemble (LSS_{2500}) and b) CV ensemble (LSS_{100}) with the corresponding marginal distributions. The marginal distributions contain values of the complete set of 112573 'land' grid cells for which LSS is estimated and are scaled by their peak for visualization. (Bottom) Comparison of the c) ensemble average and d) standard deviation of LSS_{2500} and LSS_{100}. The 1-1 line (red, dashed) is shown as reference.

The uncertainty $\sigma_{LSS_{2500}}$ is large for areas with intermediate $\overline{LSS}_{2500}$, whereas very high or low $\overline{LSS}_{2500}$ typically have a smaller associated $\sigma_{LSS_{2500}}$.

310   Figure 5 illustrates the ensemble LSS_{2500} distribution for 20 randomly sampled landslide presence and absence grid cells. Even though we quantify the uncertainty with a $\sigma_{LSS_{2500}}$, the distributions are mostly non-gaussian. Most displayed landslide presence (absence) grid cells have LSS distributions ranging at the upper (lower) end of the interval (0,1). Grid cells 1, 7 and 18, however, exhibit a very wide distribution that seems disconnected from the absence (1, 17) or presence (18) of a landslide.
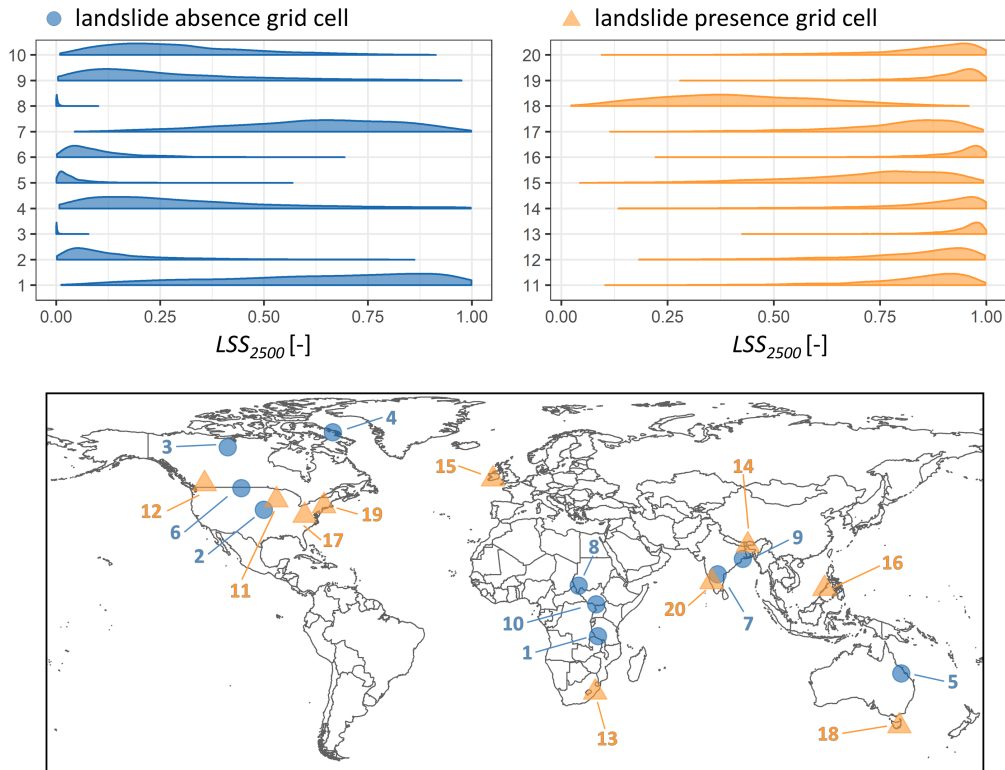
Figure 5. Distribution of ensemble member *LSS* values (LSS_{2500}) within sample grid cells for select landslide presence (light orange triangle on map) and absence (blue circle on map) grid cells. Please note that the distributions (top) all contain 2500 *LSS* ensemble members and are merely scaled by their peak to avoid overlaying (large peak) or invisible (small peak, but wide distribution) curves.

The ROC curves for ensemble average $\overline{LSS}_{2500}$ are shown in Fig. 6, with the curves for Russia (AUC: 0.92) and Italy (AUC: 0.91) being closest to the upper left corner, and that for Africa being a little further from this optimum (AUC: 0.84). The $\overline{LSS}_{2500}$ map hence very well captures the landslide patterns over all three regions.

4.3 Impact of input perturbations

The above discussion of the full ensemble LSS_{2500} includes perturbations to the predictor variables on top of the CV ensemble LSS_{100} obtained by the CV techniques alone. Figure 4a and b show that the *LSS* uncertainty is a function of the average *LSS* values and that $\sigma_{LSS_{2500}}$ is typically higher than $\sigma_{LSS_{100}}$. Figure 4d shows that the differences between $\sigma_{LSS_{2500}}$ and $\sigma_{LSS_{100}}$ are smallest for the very high and low $\sigma_{LSS_{100}}$. However, Figure 4c shows that the ensemble averages $\overline{LSS}_{2500}$ and $\overline{LSS}_{100}$ are similar, as expected from the additional zero-mean predictor variable perturbation. The values of $\overline{LSS}_{2500}$ are slightly smaller than those of $\overline{LSS}_{100}$, except for very small $\overline{LSS}$ (< 0.1).
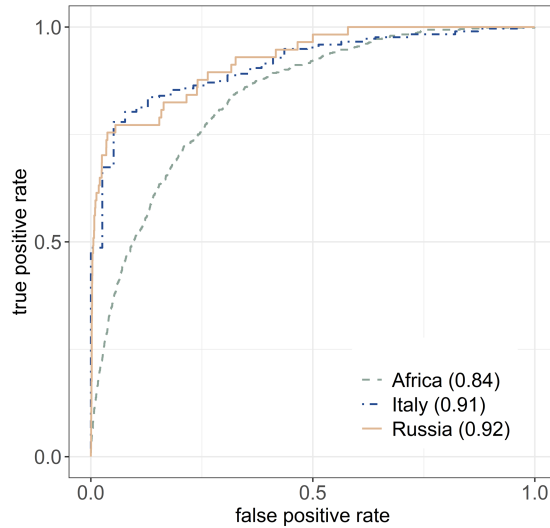
Figure 6. ROC curves of full ensemble average LSS ($\overline{LSS}_{2500}$) for validation inventories from Russia, Italy and Africa. Corresponding AUC values are denoted in brackets.

Figure 7 shows boxplots of the AUC values for individual members of the CV ensemble (LSS_{100}) and the full ensemble
325   (LSS_{2500}) compared against the according CV test subsets, as well as the independent validation inventories. Note that LSS_{100}
is a subset of LSS_{2500}. The median AUC value is lower for LSS_{2500} than for LSS_{100} for all reference data. Despite this shift,
a number of the LSS_{2500} ensemble members also perform better than any of those from LSS_{100}. The intention is not for
the individual ensemble members to have the best prediction, but rather for the ensemble average $\overline{LSS}$ to be best: clearly the
ensemble mean performs better than the majority of the individual ensemble members. We find AUC values for these $\overline{LSS}_{2500}$
330   and $\overline{LSS}_{100}$ (dots on the figure) to be practically the same (Fig. 4c)

5   Discussion

5.1   Selected predictor variables

For the global *LSS* prediction of this study, the mean CTI per grid cell is the most important predictor variable. Mean and
maximum slope within a grid cell are selected less often as the first predictor variable, but one of the two is still included in
335   nearly every MELR model. We attribute the primary importance of CTI to the fact that our model is trained with data from
hydrologically-triggered landslides (Kirschbaum et al., 2010, 2015), which do not uniquely occur on steep slopes. The CTI
intrinsically contains information on the potential hydrological conditions of the site (through the catchment area) as well as
its slope. In line with our study, Emberson et al. (2021) found that the CTI is a strong predictor of rainfall-induced landslides
for a number of inventories in the tropics and subtropics. Earlier global *LSS* maps by Nadim et al. (2006), Hong et al. (2007)
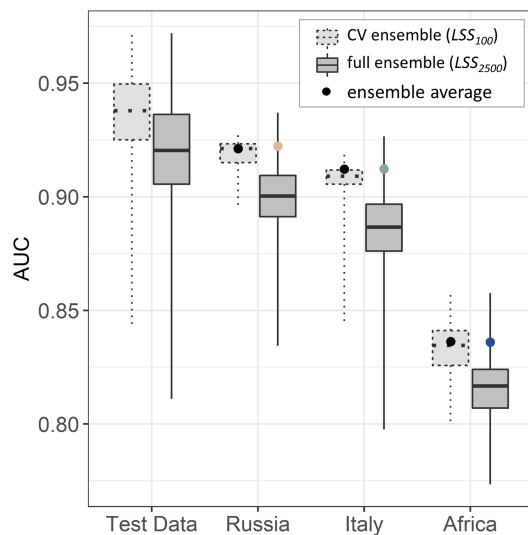
Figure 7. Distribution of AUC for model fitting performance (test data) and model prediction performance (based on independent validation inventories from Russia, Italy and Africa). Boxplots are shown for CV ensemble members (LSS_{100}) and full ensemble members (LSS_{2500}, including CV ensemble members), with whiskers extending from minimum to maximum AUC. AUC values for ensemble averages are displayed as points (black: $\overline{LSS}_{100}$, coloured: $\overline{LSS}_{2500}$). The latter correspond to the ROC curves shown in Fig. 6.

340 and Stanley and Kirschbaum (2017) primarily used slope information, while Lin et al. (2017) use relative relief. The latter is comparable to the standard deviation of elevation, which is selected in more than 25% of the models of our study.

Long-term median surface soil moisture was most frequently selected as the second predictor variable and part of more than 80% of all models. The positive connection to *LSS* reflects the fact that hydrologically-triggered landslides mostly occur in humid regions where the soil is often wet and rainfall can more easily destabilize a slope. The close relation between surface

345 soil moisture and rainfall characteristics is probably the reason for its preferred selection compared to deeper layer soil moisture variables. The high correlation between surface soil moisture and both rainfall and deeper layer soil moisture variables prevents that the latter two would be selected during one model creation (see Sect. 3.2). The preference for median surface soil moisture over average rainfall might be due to the less extreme values in soil moisture (quasi-normal distribution) compared to the highly non-normal distribution of rainfall, but could also reflect that surface soil moisture intrinsically contains additional information

350 on the soil characteristics. It can be interpreted as a proxy or integrator of rainfall patterns, soil and possibly also vegetation characteristics. Similar to surface soil moisture, a positive relation of *LSS* is found for the (inter-quartile) range of evaporation. This accounts for regions with strong seasonality in rainfall and in the associated evaporation over wet soils.

In earlier global *LSS* maps, Nadim et al. (2006) and Lin et al. (2017) included information on the soil moisture in the form of a soil moisture index by Willmott and Feddema (1992)) that distinguishes 'wet' and 'dry' climates. Lin et al. (2017) found

355 this index to be the most important predictor variable. Broeckx et al. (2018) include climatological average annual rainfall as a

predictor variable for *LSS* over Africa. At the global scale, the use of climatological statistics of hydrometeorological variables for *LSS* has not been tested before. It is important to note that such long-term statistics are meant to remain constant in time for global *LSS* estimation (by definition), but they also offer the possibility to recompute and refine *LSS* estimates in an era of climate change.

360   We did not find significant contributions of lithological predictor variables. For Africa, Broeckx et al. (2018) found a (limited) impact of the presence of unconsolidated sediments and siliclastic sedimentary rocks on *LSS*. Stanley et al. (2021) found the lithology (regrouped from GLiM) to be the least important factor. While local lithology plays a vital role for landslide occurrence, the large data uncertainty and often very broad definitions (as for example elaborated by Campforts et al. (2020) in a different context) hinder meaningful contributions to *LSS* assessment, even for smaller scale studies. This might also explain

365   why, instead, PGA was favoured as a proxy for structural weakening during the variable selection. The one-time selection of the fraction of land within a grid cell, with a negative β-value assigned, reflects that coastal or shore areas with a low land fraction are more prone to landslides (higher *LSS*).

    Overall, the selected predictor variables, as well as the assigned β-values are in line with general geomorphologic understanding and previous studies. We acknowledge, however, that not all possible predictors for landslides were included in the

370   analysis. For example, land cover and land use were not explicitly included (although they are implicitly included in the climatological statistics of soil moisture, runoff and evaporation). Forest has been found to be less susceptible to landslides than non-forested areas in some regional studies (Sidle and Bogaard, 2016; Knevels et al., 2021; Depicker et al., 2021; Steger et al., 2020), although Stanley and Kirschbaum (2017) pointed out that landslides are also simply more easily observed in non-forested areas. Land cover and land use change, e.g. deforestation and urbanization (possible slope undercutting and changes

375   in the natural drainage system of hillslopes) are also known to increase propensity for landslides (Dille et al., 2019; Depicker et al., 2021). Stanley and Kirschbaum (2017) include forest loss and presence of roads as predictor variables for their global susceptibility map. With the expanding human presence, such predictor variables would require temporal updates and need further research for global applications.

5.2   Full ensemble results

380   The spatial patterns of the full ensemble average *LSS* ($\overline{LSS}_{2500}$, see Fig. 3) agree well with those of the categorical *LSS* maps by Stanley and Kirschbaum (2017) at 1 km resolution and Lin et al. (2017) at $0.5°$ resolution, shown in Fig. 8a and b. Figure 8 c and d show the distribution of the continuous 36-km $\overline{LSS}_{2500}$ per *LSS* class of these two reference maps. In comparing the maps, we find a larger area covered by high $\overline{LSS}_{2500}$ for example in the Eastern United States, Latin America, Mediterranean Europe, India, South-East Asia and New Zealand. At the same time, $\overline{LSS}_{2500}$ shows much less variation than the map by

385   Stanley and Kirschbaum (2017) within large deserts (Sahara, Arabian peninsula and central Australia). This might be a result of the coarser spatial resolution, but is also attributable to the fact that $\overline{LSS}_{2500}$ is strongly governed by hydrological predictor variables apart from the typical geomorphological ones. With a very large proportion of the lowest *LSS* class, Lin et al. (2017) have even less variation within these areas than $\overline{LSS}_{2500}$.
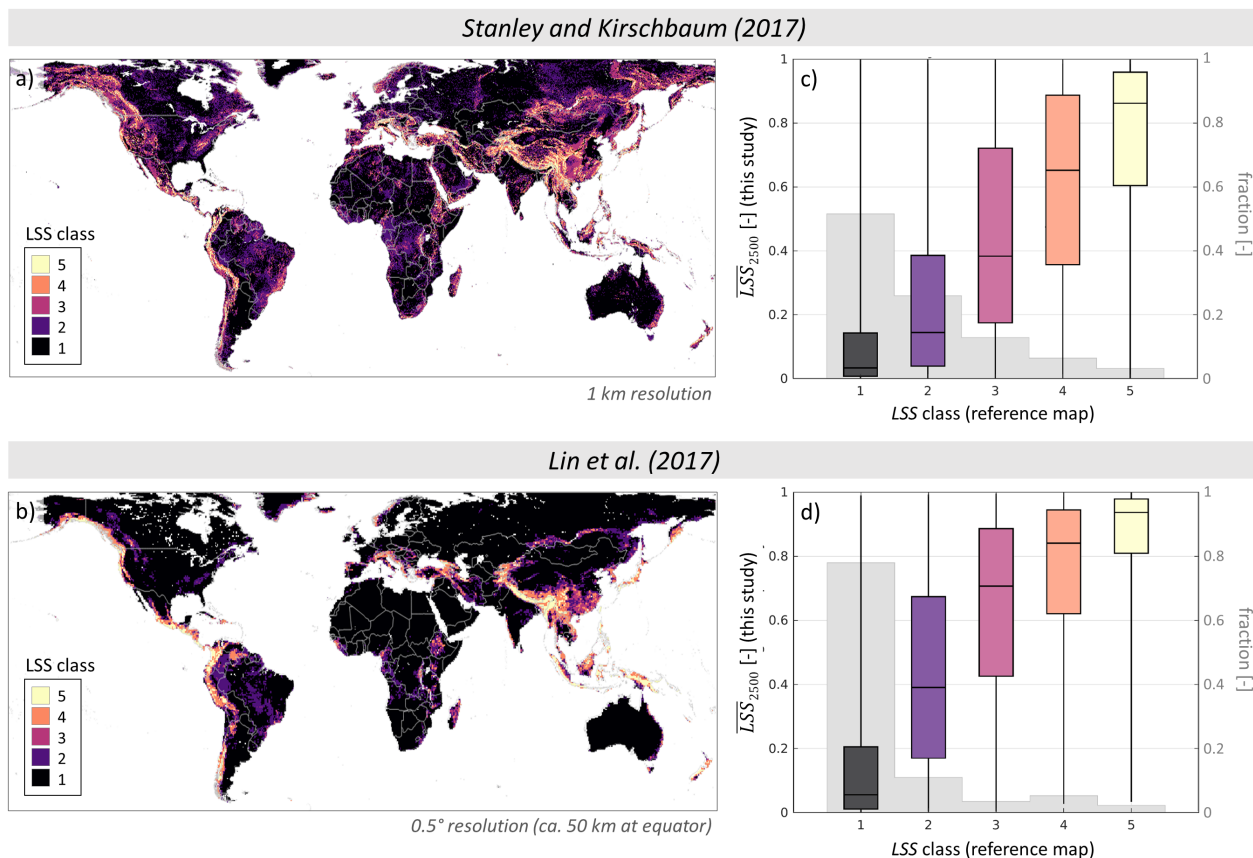
Figure 8. Comparison of $\overline{LSS}_{2500}$ against existing global categorical *LSS* maps by (a) Stanley and Kirschbaum (2017) and (b) Lin et al. (2017). Boxplots show $\overline{LSS}_{2500}$ values extracted from the nearest 36-km grid cell for each (c) 1-km and (d) 0.5^o grid cell in the reference map per *LSS* class. Whiskers extend from minimum to maximum $\overline{LSS}_{2500}$. Boxplots are underlain with the fractions of the reference map *LSS* classes (grey). Note that both reference maps start off from continuous *LSS* values but use very different thresholds for the class definitions: Stanley and Kirschbaum (2017) set breakpoints at [0.11,0.49,0.67,0.75], defined so that each category contains twice as many grid cells as the next highest, whereas Lin et al. (2017) set breakpoints at [0.4,0.6,0.7,0.9], following Guzzetti et al. (2006) and Van Den Eeckhaut et al. (2012).

These realistic spatial distributions of $\overline{LSS}_{2500}$ are supported by the AUC values calculated for this ensemble average (dots in Fig. 7). The lower AUC value for Africa can be attributed to the fact that the inventory comprises also very old landslides from very different climatic conditions. In general though, these AUC values are in line with those of Stanley and Kirschbaum (2017) and Lin et al. (2017), who reported AUC between 0.6 and 0.9, and around 0.9, respectively.

Figure 5 shows that the distributions of *LSS* ensemble members within one grid cell could have a very wide range. Even though in this figure we only selected locations within English-speaking countries and excluded unreliable absence grid cells

395 (see Sect. 2.1), it is still possible that an absence grid cell could experience a landslide, even if none has been reported in the GLC. A prominent example of this are absence grid cells 1 and 7, located in the East African Rift and India, respectively. Both grid cells have no reported landslide, but very wide *LSS* distributions, with relatively high *LSS* values. This discrepancy between prediction and observation could indicate the need to visit this location for landslide research. At the same time, landslide presence grid cell 18 also has a very wide *LSS* distribution with a rather low average. This could either indicate that a

400 non-hydrological process caused the landslide (misclassification) or that specific unrepresented features are present within the grid cell area. Overall, we find an average $\overline{LSS}_{2500}$ of 0.18 (0.82) for landslide absence (presence) grid cells (as displayed in Fig. A1) which makes us confident in our classification of these grid cells.

Calculating the ensemble standard deviation of these distributions ($\sigma_{LSS_{2500}}$) is a good measure of *total prediction uncertainty* associated with the $\overline{LSS}_{2500}$ for one grid cell. The $\sigma_{LSS_{2500}}$ is typically small for distributions at either end of the *LSS*

405 interval (0,1), resulting in the parabolic pattern as displayed in Fig. 4a-b. This pattern has also been found for local assessments (Guzzetti et al., 2006; Depicker et al., 2020)) and holds for Broeckx et al. (2018) over Africa as well (visual comparison of two maps). The reasons for this relationship between $\overline{LSS}_{2500}$ and $\sigma_{LSS_{2500}}$ are twofold: (i) The classification algorithm works best for extreme environmental conditions, such as very steep slope or completely flat areas and has a strongly nonlinear, asymptotic behaviour (logistic regression), and (ii) the predictions are limited to the interval (0,1), restraining the opportunity

410 for deviations at the extremes to one side. A comparison of $\sigma_{LSS_{2500}}$ with independent global estimates is currently not possible for lack of uncertainty estimates (Nadim et al., 2006; Hong et al., 2007; Stanley and Kirschbaum, 2017; Lin et al., 2017). However, a comparison with the standard deviations retrieved during the process of random CV for the continental *LSS* map of Africa by Broeckx et al. (2018) (i.e. not accounting for the *total uncertainty*) reveals that the patterns are very similar, but with less (more) variation in $\sigma_{LSS_{2500}}$ for the very arid (humid) regions.

415 ## 5.3 Impact of input perturbations

In this study, we add predictor variable perturbations to the CV approach in order to obtain a more reliable estimate of the *total prediction uncertainty* from the resulting full ensemble. By design, the zero-mean input perturbation does only marginally affect the ensemble $\overline{LSS}$ (see Fig. 4). Slightly increased (decreased) $\overline{LSS}_{2500}$ at the lower (upper) limits can be attributed to the resampling of predictor variable values if they exceed the definition interval of rescaled predictor variables (0,1). Overall,

420 this introduced bias remains small.

The AUC analysis (Fig. 7) shows that the ensemble averages perform much better than individual ensemble members, and that $\overline{LSS}_{2500}$ and $\overline{LSS}_{100}$ perform equally well. Not shown is that the BS (Equation 2) decreases (i.e. improves) for LSS_{2500} in comparison to LSS_{100} where *LSS* is not very close to the observation already (landslide presence and absence). This effect is, however, not visible in the AUC comparison (spatial accuracy) for the validation data in Russia, Africa and Italy because the

425 grid cells with BS improvement only make up for ∼8%, ∼9% and ∼18% respectively. The AUC values of ensemble averages remain practically the same, and an *LSS* model without predictor perturbations would hence suffice for a general insight in the global spatial *LSS* pattern.

That the individual ensemble member *LSS* maps of LSS_{2500} (based on perturbed variables) have lower median AUC values than LSS_{100} is logical: the model equations are tailored to the original predictor variable values so that they are optimally combined into an *LSS* prediction. Any change of these variables could deteriorate the outcome. This is, however, no lack in quality of the ensemble, but rather a side effect. We do not use the individual ensemble members but their average as an *LSS* prediction, for which we find practically unchanged spatial accuracy between CV ensemble and full ensemble.

By tuning the predictor variable perturbations to match the *total ensemble prediction uncertainty* to the observed actual uncertainty, we are able to provide statistically reliable uncertainty estimates for the predicted average *LSS*, even in places where landslide observations are unavailable. As stated before, this optimized spread is introduced to the input variables, but does not actually reflect the input errors only: it also compensates for other uncertainty sources that are not specifically addressed, incl. spatial representativeness error, and uncertainties introduced by heuristic decisions along the way, such as the choice of the statistical model, etc. Explicitly accounting for these error sources would require dedicated analyses (as for example conducted by Depicker et al. (2020)). Because Zêzere et al. (2017) found that the choice of spatial mapping unit influences *LSS* estimates stronger than the choice of statistical model, we do not expect that our results would fundamentally change for approaches other than MELR. Future research could explore the additional information, such as landslide sizes, types or the frequency of occurrence per grid cell instead of reducing the data to landslide presence and absence. For the latter, one would need to find ways to counteract the English-language and economic bias of the GLC which is more pronounced when using the actual number of reports instead of the presence-absence method chosen in this study.

6   Conclusions

This study presents the first global landslide susceptibility (*LSS*) map directly developed to be compatible with satellite soil moisture products retrieved from passive microwave sensors, i.e. at a spatial resolution of 36 km. The novel method of combining blocked random CV (B-CV) and predictor variable perturbations results in a reasonable assessment of the associated *total prediction uncertainty*. For each grid cell, we estimate 2500 individual *LSS* values ('full ensemble') that are summarized by the ensemble average *LSS* ($\overline{LSS}$) and standard deviation (σ_{LSS}, i.e. the uncertainty). Together, these *LSS* statistics can provide unprecedented information for subsequent global probabilistic spatio-temporal landslide modeling, and statistical combination of the *LSS* and soil moisture estimates, each with their respective uncertainties. Furthermore, the *LSS* maps have the potential to discern areas that deserve more attention for landslide detection.

A mixed effects logistic regression (MELR) is used as the model structure to relate environmental predictor variables to spatial landslide likelihoods. The objectively selected predictor variables are mainly related to slope and hydrology, in line with the expectations for hydrologically-triggered landslides. The odds of landslide occurrence were found to (i) decrease with increasing compound topographic index (CTI), which depends on the ratio of catchment area and slope and (ii) increase with increasing slope, peak ground acceleration (PGA) and long-term climatological statistics of surface soil moisture (median and 99th percentile) or range of evaporation. The inclusion of long-term statistics of hydrometeorological variabels enables future investigations into possible shifts in *LSS* due to climate change.

The map of the full ensemble $\overline{LSS}$ reproduces global patterns of *LSS* as presented in previous global studies well. The performance assessment yields area under the ROC curve (AUC) values of 0.92, 0.91 and 0.84 for independent data from Russia, Italy and Africa, respectively. The uncertainty σ_{LSS} is largest for intermediate $\overline{LSS}$. High predicted *LSS* at (reliable) landslide absence grid cells might furthermore indicate regions that could benefit from future landslide detection and research.

465   For the ensemble perturbations of the selected predictor variables we use a perturbation magnitude of 15% to 20%, linearly proportional to the variation of elevation within a grid cell. The magnitude is chosen to match the *total predicted ensemble uncertainty* with the observed actual uncertainty relative to data from the Global Landslide Catalog (GLC). Adding these perturbations does not linearly propagate into the ensemble spread due to the asymptotic nature of logistic regression. It increases the ensemble spread for locations of intermediate $\overline{LSS}$ while having negligible impact where $\overline{LSS}$ is close to its lower

470 or upper limit. The ensemble $\overline{LSS}$ and its spatial accuracy (AUC) remain practically unchanged by the ensemble perturbations, but AUC values of these average predictions are always much better than that of individual ensemble realizations. In short, these novel methods explicitly focus on the uncertainty quantification. The availability of global reliable uncertainty estimates is an unprecedented new contribution to the suite of global *LSS* maps, and it will support stochastic landslide hazard modeling.

Code and data availability.   For most of the landslide and environmental predictor data we refer the reader to the provided sources. Source
475 code and climatological statistics of hydrological parameters in netCDF format can be obtained by contacting the authors. The resulting full *LSS* ensemble is available as a netCDF file as well and will be publicly available after the acceptance of this paper.

Appendix A

A1   Landslide absence sampling

Figure A1 shows the N_{LS}=3757 landslide locations based on data from the GLC aggregated to the 36-km EASEv2 (sec-
480 tion 2.1). Landslide absence grid cells are sampled between a minimum (buffer) and maximum distance around known land-slide locations (N_{noLS}=25417). These distances can be based on either heuristic choices (Van Den Eeckhaut et al., 2012; Lin et al., 2017; Knevels et al., 2020) or empirical approaches (Zhu et al., 2017; Nowicki Jessee et al., 2018; Lucchese et al., 2021).

     For our global study, we set a buffer based on the probability for any two landslide locations from the GLC to be reported within a specific distance interval for 100 spatially defined clusters (k-means-clustering (Lloyd, 1982) on latitude and lon-
485 gitude). Figure A2 shows that the frequency of encountering two landslide locations decreases for larger distances and can be characterized by a Poisson exponential fit. In line with the definition of autocorrelation length (Gaspari and Cohn, 1999), we define the 'characteristic distance' between two landslides as the distance where the probability to meet another landslide drops by 1/e. We use this characteristic distance of 221.43 km or ∼6 36-km grid cells (median of characteristic distances retrieved for 50 repetitions of the clustering) as a buffer around landslide locations. The maximum distance around a landslide
490 is subsequently defined as 2.5 times this characteristic distance (553.58 km, ∼15 grid cells), borrowing from the data assimi-
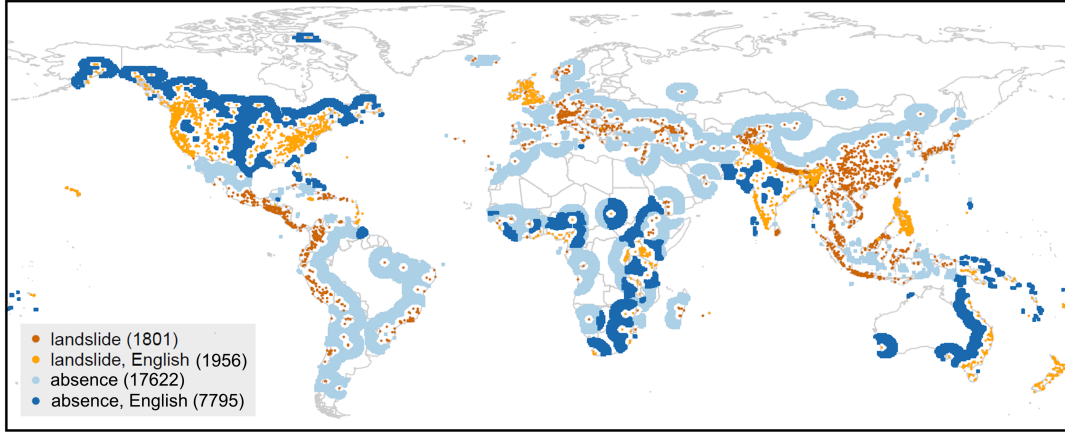
Figure A1. Spatial distribution of landslide presence (shade of orange) and absence (shade of blue) grid cells at 36-km resolution, for English speaking countries (light orange and dark blue) and non-English speaking countries (dark orange and light blue). White indicates grid cells that are excluded during the model creation process (buffer and maximum radius around landslide location, see sect. 2.1). The numbers are the sum of each subgroup of grid cells.

lation community where 2.5 times the autocorrelation length is a measure for absence of correlation (Gaspari and Cohn, 1999; De Lannoy, 2006; De Lannoy et al., 2010).

Landslide absence grid cells are hence selected from 7 to 15 grid cells around a landslide presence grid cell (blue grid cells in Fig. A1). These distances are inevitably much larger than those found in literature for finer-scale studies, because 495 autocorrelation lengths are scale-dependent and the retrieved characteristic distance is influenced by the spatial extent, or the definition of the clusters in our case.

A2   Input perturbation and optimization

For a reliable assessment, the *total ensemble prediction uncertainty* of the obtained ensemble average $\overline{LSS}$ map ideally should match the observed actual uncertainty. The first can be defined for a single location by the standard deviation (σ) among the 500 LSS ensemble members (LSS_i, with $i = 1, ..., N_{ens}$), as also displayed in sect. 4 and Fig. 3. Similarly, it is possible to assess the according variance (σ^2), referred to as ensemble spread (*ensp*):

$$ensp = \frac{1}{N_{ens}} \sum_{i=1}^{N_{ens}} (LSS_i - \overline{LSS})^2 \tag{A1}$$

The observed actual uncertainty at a single location is defined as the difference between $\overline{LSS}$ and the aggregated landslide observations from the GLC (o), referred to as the ensemble skill (*ensk*):

505 $ensk = (\overline{LSS} - o)^2 \tag{A2}$
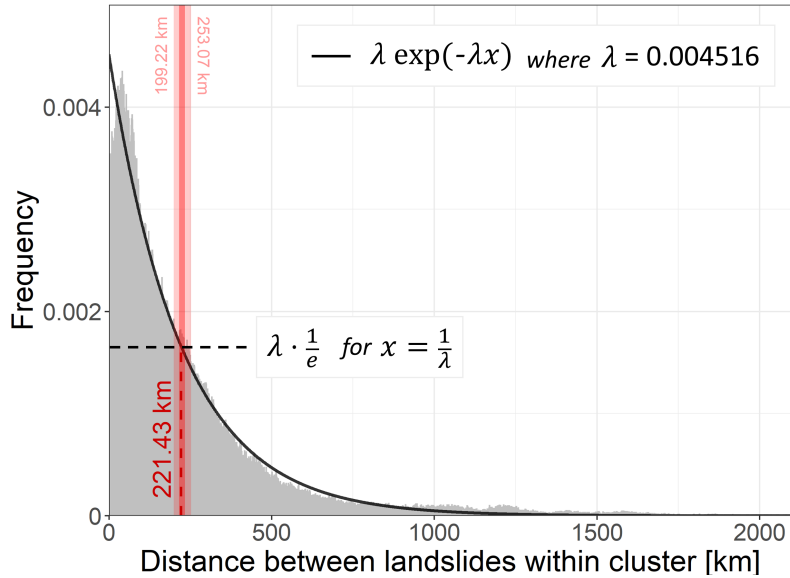
Figure A2. Histogram of distances [km] between landslides within a k-means cluster (for 100 clusters across the globe) of the GLC (grey) and Poisson exponential fit (black line) to retrieve the characteristic landslide distance (red). The red dashed line indicates median characteristic landslide distance from 50 repetitions of the k-means clustering, with the smallest and largest characteristic distance indicated by the light red bar and numbers at top.

where o is 1 (0) in case of a landslide presence (absence) grid cell. The smaller *ensk*, the closer the predicted $\overline{LSS}$ to the observation. This is essentially a Brier Score (see Equation 2) for one single grid cell. (Wilks, 2011).

The optimization of the uncertainty estimates entails tuning of *ensp* to match *ensk*. In this study, this is done by varying the perturbation magnitude that is added to the input variables (see sect. 3.2). Talagrand et al. (1997) defined spread-skill relationships that allow to verify the statistical consistency between the assumed uncertainty (chosen perturbation) and the actual 'observed' uncertainty based on the ergodicity principle. Over a large number of realizations, i.e. for large enough ensembles, $\langle ensk - ensp \rangle \to 0$ or

$$\frac{\langle ensk \rangle}{\langle ensp \rangle} \to 1 \Leftrightarrow log\left(\frac{\langle ensk \rangle}{\langle ensp \rangle}\right) \to 0 \tag{A3}$$

where $\langle . \rangle$ denotes the average. In most hydrological or meteorological applications, this is the temporal average within one grid cell. As this is not applicable for the static *LSS* data, we consider (i) spatial averages $\langle ensk \rangle / \langle ensp \rangle$ per *LSS* interval as well as (ii) the distribution of individual $ensk/ensp$ per grid cell. Both should only be performed over grid cells with reliable information about landslide presence or absence (see Appendix A1). Note that this definition of $\langle ensk \rangle$ corresponds to the definition of the Brier Score as given in sect. 3.2.

We tested various magnitudes of perturbations to the rescaled predictor variables either by using (i) a globally constant standard deviation or (ii) a standard deviation proportional to the topographic complexity (i.e. the variation within a grid cell,
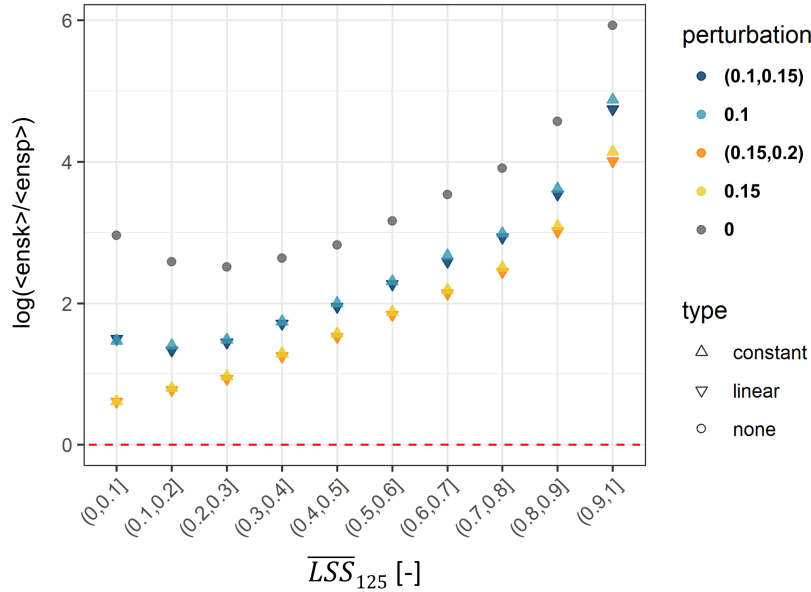
Figure A3. Spread-skill relationship $log(\langle ensk\rangle/\langle ensp\rangle)$, stratified per ensemble average LSS ($\overline{LSS}_{125}$). The optimum of 0 is indicated by red dashed line. Shapes indicate the type and colours the magnitude (constant) and interval (linear) of perturbation.

here the standard deviation of elevation). A range of possible perturbation options was tested for a partial ensemble (LSS_{125}, i.e. no repetition of landslide absence sampling as illustrated in Fig. 1). Figure A3 shows $log(\langle ensk_{LSS_{125}}\rangle/\langle ensp_{LSS_{125}}\rangle)$ for 10 intervals of $\overline{LSS}_{125}$ and two examples of constant and linear perturbations. Adding any of the four perturbations brings $log(\langle ensk_{LSS_{125}}\rangle/\langle ensp_{LSS_{125}}\rangle)$ values closer to zero, i.e. improves the spread-skill relationship, compared to results without

525   a perturbation (LSS_5, single CV ensemble). Linear perturbations introduce larger spread in areas of higher $\overline{LSS}_{125}$ resulting in $log(\langle ensk_{LSS_{125}}\rangle/\langle ensp_{LSS_{125}}\rangle)$ closer to zero than constant perturbations, and are therefore preferred here.

We futher analyze the distribution of individual *ensp* and *ensk* across all grid cells in Fig. A4 (top), stratified for landslide presence and absence. Ideally, *ensp* versus *ensk* should stay close to the 1-1 line. Adding a perturbation to the predictor variables (Fig. A4 c in comparison to a) nudges the distribution in this direction, but fails to do so for large *ensk*: a large *ensk* results

530   from a large difference between $\overline{LSS}_{125}$ and landslide observation (*o*), and often coincides with very small *ensp*. This can be attributed in part to the incompleteness of the GLC (missing observations in a very susceptible area) and the coarse spatial resolution of this study (one very susceptible location surrounded by dominantly non-susceptible area within grid cell). Note also that the logistic regression (see Equation 1) does not linearly propagate the perturbations of predictor variables into the resulting *LSS* values, especially not at the edges of the definition interval (0,1). Accepting this tail of the distribution as an

535   unavoidable characteristic, we further analyze the histogram of grid cell wise $log(ensk/ensp)$ as displayed in Fig. A4 b and d. An optimal perturbation would result in median $log(ensk/ensp)$ close to zero and a small inter-quartile range (IQR). We

therefore define the optimal perturbation for a minimum Euclidean distance (d) between the point $(median|IQR)$ and $(0|0)$, averaged over the distribution of observed landslide presences and absences ($o = 0, 1$):

$$\bar{d} = \frac{1}{2} \sum_{o=0,1} (median^2 + IQR^2)_o \qquad (A4)$$

540   The $\bar{d}$ for a range of possible linear perturbation options for LSS_{125} is summarized in Fig. A4e. The optimal perturbation (smallest $\bar{d}$) scales the applied standard deviation according to topographic complexity, represented by the standard deviation of elevation within a grid cell, between $(0.15, 0.2)$, i.e. between 15% and 20%. Fine tuning of the standard deviation is left for future work, but could involve other variables or transformations thereof or different amounts of perturbations per predictor variable.
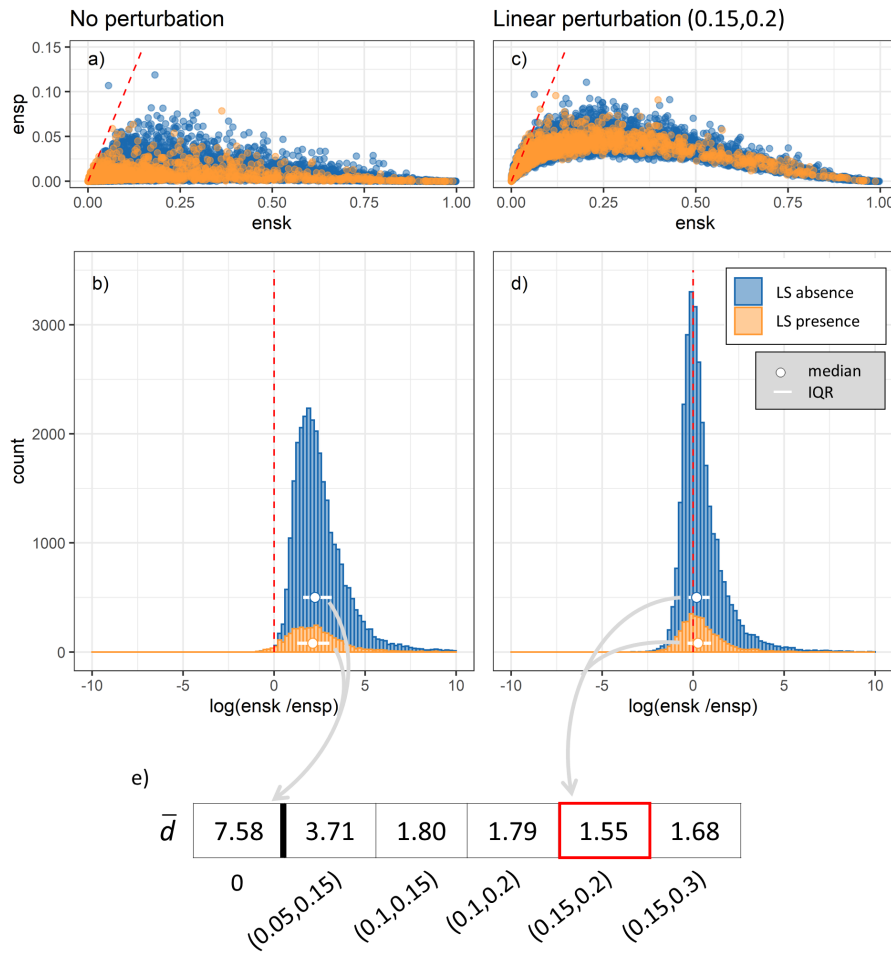
Figure A4. Spread-skill relationship per grid cell with the optimum indicated by the red dashed lines: (top; a,c) scatter plots of *ensk* against *ensp*, (middle; b,d) histograms of $log(ensk/ensp)$, stratified for landslide presence and absence (between buffer and maximum distance). (Bottom; e) summary of the average Euclidean distance $\bar{d}$ for all applied linear perturbations with the optimum framed in red. Shown are results for a-b) without perturbation of predictor variables (LSS_5), and c-d) for linear perturbation of predictor variables within the interval (0.15,0.2) (LSS_{125}). In other words, (a-b) account for *model uncertainty* alone whereas (c-d) account for the *total uncertainty* (see Fig. 1).

545   *Author contributions.* AF designed the *LSS* assessment setup, created the code and conducted the analysis, supervised by GDL and JP along the way. GDL provided scientific guidance for all steps of this study, with special focus on the input perturbation and optimization. MB provided guidance for the CV approaches. JP and MV provided topical expertise for interpretation of results. All co-authors provided guidance on the study's content and contributed to the paper.

Competing interests. The authors declare that they have no conflict of interest.

550 *Acknowledgements.* We thank Thomas Stanley for providing data, feedback and recommendations. We also thank Jente Broeckx for his input, Bianca Drepper for the support in the data preparations and two anonymous reviewers for their valuable review comments. We additionally thank Luca Brocca for being part of the advisory committee of AF. The computational resources (High Performance Computing) and services used in this work were provided by the VSC (Flemish Supercomputer Center), funded by KU Leuven (C14/16/045), FWO (1512817N) and the Flemish Government. AF was funded by FWO-G0C8918N.

555 **Abbreviations**

N_{LS} number of landslide locations, i.e. landslide presence grid cells

N_{noLS} number of landslide absence grid cells

LSS landslide susceptibility

ensk ensemble skill

560 *ensp* ensemble spread

AIC Akaike information criterion

AUC area under the ROC curve

B-CV blocked random CV

BS Brier Score

565 **CLSM** Catchment Land Surface Model

CTI compound topographic index

CV cross validation

DEM digital elevation model

EASEv2 Equal-Area Scalable Earth version 2

570 **GLC** Global Landslide Catalog

GLiM Global Lithological Map

GMTED2010 Global Multi-resolution Terrain Elevation Data 2010

GRIP Global Roads Inventory Project

GSHAP Global Seismic Hazard Assessment Project

575 **GSHM** Global Seismic Hazard Map

GSWP-2 Second Global Soil Wetness Project

GTOPO30 USGS global elevation model

HWSD1.21 Harmonized World Soil Databank version 1.21

IQR inter-quartile range

580 **LHASA** Landslide Hazard Assessment for Situational Awareness

LRC Landslide Reporter Catalog

MELR mixed effects logistic regression

MERRA-2 Modern-Era Retrospective analysis for Research and Applications, Version 2

PGA peak ground acceleration

585 **R-CV** random CV

RND average road network density

ROC Receiver Operating Characteristic

SMAP Soil Moisture Active Passive

SMOS Soil Moisture Ocean Salinity

590 **SRTM** Shuttle Radar Topography Mission

STATSGO2 State Soil Geographic project

USGS United States Geological Survey

VIF Variance Inflation Factor

References

Bates, D., Mächler, M., Bolker, B., and Walker, S.: Fitting Linear Mixed-Effects Models Using lme4, Journal of Statistical Software, 67, 1–48, https://doi.org/10.18637/jss.v067.i01, 2015.

Blöschl, G. and Sivapalan, M.: Scale Issues in Hydrological Modelling: A Review, Hydrological Processes, 9, 251–290, https://doi.org/10.1002/hyp.3360090305, 1995.

Bosilovich, M. G. L.: MERRA-2: File Specification, Tech. rep., 2015.

Brenning, A.: Spatial Prediction Models for Landslide Hazards: Review, Comparison and Evaluation, Natural Hazards and Earth System Science, 5, 853–862, 2005.

Broeckx, J., Vanmaercke, M., Duchateau, R., and Poesen, J.: A Data-Based Landslide Susceptibility Map of Africa, Earth-Science Reviews, 185, 102–121, https://doi.org/10.1016/j.earscirev.2018.05.002, 2018.

Broeckx, J., Rossi, M., Lijnen, K., Campforts, B., Poesen, J., and Vanmaercke, M.: Landslide Mobilization Rates: A Global Analysis and Model, Earth-Science Reviews, 201, 102 972, https://doi.org/10.1016/j.earscirev.2019.102972, 2020.

Calvello, M. and Pecoraro, G.: FraneItalia: A Catalog of Recent Italian Landslides (Version 2.0), 2, https://doi.org/10.17632/zygb8jygrw.2, 2020.

Campforts, B., Vanacker, V., Herman, F., Vanmaercke, M., Schwanghart, W., Tenorio, G. E., Willems, P., and Govers, G.: Parameterization of River Incision Models Requires Accounting for Environmental Heterogeneity: Insights from the Tropical Andes, Earth Surface Dynamics, 8, 447–470, https://doi.org/10.5194/esurf-8-447-2020, 2020.

Crozier, M.: 7.26 Mass-Movement Hazards and Risks, in: Treatise on Geomorphology, pp. 249–258, Elsevier, https://doi.org/10.1016/B978-0-12-374739-6.00175-5, 2013.

De Lannoy, G. J. M.: Assimilation of Soil Moisture Observations into a Spatially Distributed Hydrologic Model, Ph.D. thesis, Ghent University, 2006.

De Lannoy, G. J. M., Reichle, R. H., Houser, P. R., Arsenault, K. R., Verhoest, N. E. C., and Pauwels, V. R. N.: Satellite-Scale Snow Water Equivalent Assimilation into a High-Resolution Land Surface Model, Journal of Hydrometeorology, 11, 352–369, https://doi.org/10.1175/2009JHM1192.1, 2010.

De Lannoy, G. J. M. D., Koster, R. D., Reichle, R. H., Mahanama, S. P. P., and Liu, Q.: An Updated Treatment of Soil Texture and Associated Hydraulic Properties in a Global Land Modeling System, Journal of Advances in Modeling Earth Systems, 6, 957–979, https://doi.org/10.1002/2014MS000330, 2014.

Depicker, A., Jacobs, L., Delvaux, D., Havenith, H.-B., Maki Mateso, J.-C., Govers, G., and Dewitte, O.: The Added Value of a Regional Landslide Susceptibility Assessment: The Western Branch of the East African Rift, Geomorphology, 353, 106 886, https://doi.org/10.1016/j.geomorph.2019.106886, 2020.

Depicker, A., Jacobs, L., Mboga, N., Smets, B., Van Rompaey, A., Lennert, M., Wolff, E., Kervyn, F., Michellier, C., Dewitte, O., and Govers, G.: Historical Dynamics of Landslide Risk from Population and Forest-Cover Changes in the Kivu Rift, Nature Sustainability, pp. 1–10, https://doi.org/10.1038/s41893-021-00757-9, 2021.

Dille, A., Kervyn, F., Mugaruka Bibentyo, T., Delvaux, D., Ganza, G. B., Ilombe Mawe, G., Kalikone Buzera, C., Safari Nakito, E., Moeyersons, J., Monsieurs, E., Nzolang, C., Smets, B., Kervyn, M., and Dewitte, O.: Causes and Triggers of Deep-Seated Hillslope Instability in the Tropics – Insights from a 60-Year Record of Ikoma Landslide (DR Congo), Geomorphology, 345, 106 835, https://doi.org/10.1016/j.geomorph.2019.106835, 2019.

Dormann, C. F., Elith, J., Bacher, S., Buchmann, C., Carl, G., Carré, G., Marquéz, J. R. G., Gruber, B., Lafourcade, B., Leitão, P. J., Münkemüller, T., McClean, C., Osborne, P. E., Reineking, B., Schröder, B., Skidmore, A. K., Zurell, D., and Lautenbach, S.: Collinearity: A Review of Methods to Deal with It and a Simulation Study Evaluating Their Performance, Ecography, 36, 27–46, https://doi.org/10.1111/j.1600-0587.2012.07348.x, 2013.

635 Emberson, R., Kirschbaum, D., Amatya, P., Tanyas, H., and Marc, O.: Insights from the Topographic Characteristics of a Large Global Catalog of Rainfall-Induced Landslide Event Inventories, Preprint, Landslides and Debris Flows Hazards, https://doi.org/10.5194/nhess-2021-250, 2021.

EROS: Global Topographic 30 Arc-Second Hydrologic Digital Elevation Model 1 Km, https://doi.org/10.5066/F77P8WN0, 2018.

Felsberg, A., De Lannoy, G. J. M., Girotto, M., Poesen, J., Reichle, R. H., and Stanley, T.: Global Soil Water Estimates as Landslide

640 Predictor: The Effectiveness of SMOS, SMAP, and GRACE Observations, Land Surface Simulations, and Data Assimilation, Journal of Hydrometeorology, 22, 1065–1084, https://doi.org/10.1175/JHM-D-20-0228.1, 2021.

FSBIH: Federal State Budgetary Institution "Hydrospetzgeologiya": Archive of Quarter Annual Reports of Exogenous Geological Processes on Territories of the Russian Federation, http://geomonitoring.ru/arxiv.html, 2018.

Gaspari, G. and Cohn, S. E.: Construction of Correlation Functions in Two and Three Dimensions, p. 57, 1999.

645 Giardini, D., Grünthal, G., Shedlock, K., and Zhang, P.: The GSHAP Global Seismic Hazard Map, Lee, W., Kanamori, H., Jennings, P. and Kisslinger, C. (eds.): International Handbook of Earthquake & Engineering Seismology, International Geophysics Series 81 B, Academic Press, Amsterdam, pp. 1233–1239, 2003.

Guzzetti, F., Reichenbach, P., Cardinali, M., Galli, M., and Ardizzone, F.: Probabilistic Landslide Hazard Assessment at the Basin Scale, Geomorphology, 72, 272–299, https://doi.org/10.1016/j.geomorph.2005.06.002, 2005.

650 Guzzetti, F., Reichenbach, P., Ardizzone, F., Cardinali, M., and Galli, M.: Estimating the Quality of Landslide Susceptibility Models, Geomorphology, 81, 166–184, https://doi.org/10.1016/j.geomorph.2006.04.007, 2006.

Hartmann, J. and Moosdorf, N.: The New Global Lithological Map Database GLiM: A Representation of Rock Properties at the Earth Surface, Geochemistry, Geophysics, Geosystems, 13, Q12 004, https://doi.org/10.1029/2012GC004370, 2012.

Hong, Y., Adler, R., and Huffman, G.: Use of Satellite Remote Sensing Data in the Mapping of Global Landslide Susceptibility, Natural

655 Hazards; Dordrecht, 43, 245–256, https://doi.org/http://dx.doi.org/10.1007/s11069-006-9104-z, 2007.

Juang, C. S., Stanley, T. A., and Kirschbaum, D. B.: Using Citizen Science to Expand the Global Map of Landslides: Introducing the Cooperative Open Online Landslide Repository (COOLR), PLOS ONE, 14, e0218 657, https://doi.org/10.1371/journal.pone.0218657, 2019.

Kalnay, E., Hunt, B., Ott, E., and Szunyogh, I.: Ensemble Forecasting and Data Assimilation: Two Problems with the

660 Same Solution?, in: Predictability of Weather and Climate, pp. 157–180, Cambridge University Press, Cambridge, https://doi.org/10.1017/CBO9780511617652.008, 2006.

Kirschbaum, D., Stanley, T., and Zhou, Y.: Spatial and Temporal Analysis of a Global Landslide Catalog, Geomorphology, 249, 4–15, https://doi.org/10.1016/j.geomorph.2015.03.016, 2015.

Kirschbaum, D. B., Adler, R., Hong, Y., Hill, S., and Lerner-Lam, A.: A Global Landslide Catalog for Hazard Applications: Method, Results,

665 and Limitations, Natural Hazards, 52, 561–575, https://doi.org/10.1007/s11069-009-9401-4, 2010.

Knevels, R., Petschko, H., Proske, H., Leopold, P., Maraun, D., and Brenning, A.: Event-Based Landslide Modeling in the Styrian Basin, Austria: Accounting for Time-Varying Rainfall and Land Cover, Geosciences, 10, 217, https://doi.org/10.3390/geosciences10060217, 2020.

Knevels, R., Brenning, A., Gingrich, S., Heiss, G., Lechner, T., Leopold, P., Plutzar, C., Proske, H., and Petschko, H.: Towards the Use of Land Use Legacies in Landslide Modeling: Current Challenges and Future Perspectives in an Austrian Case Study, Land, 10, 954, https://doi.org/10.3390/land10090954, 2021.

Koster, R. D., Suarez, M. J., Ducharne, A., Stieglitz, M., and Kumar, P.: A Catchment-Based Approach to Modeling Land Surface Processes in a General Circulation Model: 1. Model Structure, Journal of Geophysical Research: Atmospheres, 105, 24809–24822, https://doi.org/10.1029/2000JD900327, 2000.

Lima, P., Steger, S., and Glade, T.: Counteracting Flawed Landslide Data in Statistically Based Landslide Susceptibility Modelling for Very Large Areas: A National-Scale Assessment for Austria, Landslides, https://doi.org/10.1007/s10346-021-01693-7, 2021.

Lin, L., Lin, Q., and Wang, Y.: Landslide Susceptibility Mapping on a Global Scale Using the Method of Logistic Regression, Natural Hazards and Earth System Sciences, 17, 1411–1424, https://doi.org/10.5194/nhess-17-1411-2017, 2017.

Lin, Q., Lima, P., Steger, S., Glade, T., Jiang, T., Zhang, J., Liu, T., and Wang, Y.: National-Scale Data-Driven Rainfall Induced Landslide Susceptibility Mapping for China by Accounting for Incomplete Landslide Data, Geoscience Frontiers, 12, 101248, https://doi.org/10.1016/j.gsf.2021.101248, 2021.

Lloyd, S.: Least Squares Quantization in PCM, IEEE Transactions on Information Theory, 28, 129–137, https://doi.org/10.1109/TIT.1982.1056489, 1982.

Lucchese, L. V., de Oliveira, G. G., and Pedrollo, O. C.: Investigation of the Influence of Nonoccurrence Sampling on Landslide Susceptibility Assessment Using Artificial Neural Networks, CATENA, 198, 105067, https://doi.org/10.1016/j.catena.2020.105067, 2021.

Maes, J., Kervyn, M., de Hontheim, A., Dewitte, O., Jacobs, L., Mertens, K., Vanmaercke, M., Vranken, L., and Poesen, J.: Landslide Risk Reduction Measures: A Review of Practices and Challenges for the Tropics, Progress in Physical Geography, 41, 191–221, https://doi.org/10.1177/0309133316689344, 2017.

Meijer, J. R., Huijbregts, M. A. J., Schotten, K. C. G. J., and Schipper, A. M.: Global Patterns of Current and Future Road Infrastructure, Environmental Research Letters, 13, 064006, https://doi.org/10.1088/1748-9326/aabd42, 2018.

Nadim, F., Kjekstad, O., Peduzzi, P., Herold, C., and Jaedicke, C.: Global Landslide and Avalanche Hotspots, Landslides; Dordrecht, 3, 159–173, https://doi.org/http://dx.doi.org/10.1007/s10346-006-0036-1, 2006.

Nowicki Jessee, M. A., Hamburger, M. W., Allstadt, K., Wald, D. J., Robeson, S. M., Tanyas, H., Hearne, M., and Thompson, E. M.: A Global Empirical Model for Near-Real-Time Assessment of Seismically Induced Landslides, Journal of Geophysical Research: Earth Surface, 123, 1835–1859, https://doi.org/10.1029/2017JF004494, 2018.

Petschko, H., Brenning, A., Bell, R., Goetz, J., and Glade, T.: Assessing the Quality of Landslide Susceptibility Maps – Case Study Lower Austria, Nat. Hazards Earth Syst. Sci., 14, 95–118, https://doi.org/10.5194/nhess-14-95-2014, 2014.

Pourghasemi, H. R. and Rossi, M.: Landslide Susceptibility Modeling in a Landslide Prone Area in Mazandarn Province, North of Iran: A Comparison between GLM, GAM, MARS, and M-AHP Methods, Theoretical and Applied Climatology, 130, 609–633, https://doi.org/10.1007/s00704-016-1919-2, 2016.

R Core Team: R: A Language and Environment for Statistical Computing, R Foundation for Statistical Computing, Vienna, Austria, https://www.R-project.org/, 2020.

Reichenbach, P., Rossi, M., Malamud, B. D., Mihir, M., and Guzzetti, F.: A Review of Statistically-Based Landslide Susceptibility Models, Earth-Science Reviews, 180, 60–91, https://doi.org/10.1016/j.earscirev.2018.03.001, 2018.

705 Reichle, R. H., Liu, Q., Koster, R. D., Crow, W. T., De Lannoy, G. J. M., Kimball, J. S., Ardizzone, J. V., Bosch, D., Colliander, A., Cosh, M., Kolassa, J., Mahanama, S. P., Prueger, J., Starks, P., and Walker, J. P.: Version 4 of the SMAP Level-4 Soil Moisture Algorithm and Data Product, Journal of Advances in Modeling Earth Systems, 11, 3106–3130, https://doi.org/10.1029/2019MS001729, 2019.

Roberts, D. R., Bahn, V., Ciuti, S., Boyce, M. S., Elith, J., Guillera-Arroita, G., Hauenstein, S., Lahoz-Monfort, J. J., Schröder, B., Thuiller, W., Warton, D. I., Wintle, B. A., Hartig, F., and Dormann, C. F.: Cross-Validation Strategies for Data with Temporal, Spatial, Hierarchical,
710 or Phylogenetic Structure, Ecography, 40, 913–929, https://doi.org/10.1111/ecog.02881, 2017.

Sidle, R. C. and Bogaard, T. A.: Dynamic Earth System and Ecological Controls of Rainfall-Initiated Landslides, Earth-Science Reviews, 159, 275–291, https://doi.org/10.1016/j.earscirev.2016.05.013, 2016.

Stanley, T. and Kirschbaum, D. B.: A Heuristic Approach to Global Landslide Susceptibility Mapping, Natural Hazards, 87, 145–164, https://doi.org/10.1007/s11069-017-2757-y, 2017.

715 Stanley, T. A., Kirschbaum, D. B., Benz, G., Emberson, R. A., Amatya, P. M., Medwedeff, W., and Clark, M. K.: Data-Driven Landslide Nowcasting at the Global Scale, Frontiers in Earth Science, 9, https://doi.org/10.3389/feart.2021.640043, 2021.

Steger, S. and Glade, T.: The Challenge of "Trivial Areas" in Statistical Landslide Susceptibility Modelling, in: Advancing Culture of Living with Landslides, pp. 803–808, Springer, Cham, 2017.

Steger, S., Bell, R., Petschko, H., and Glade, T.: Evaluating the Effect of Modelling Methods and Landslide Inventories Used for
720 Statistical Susceptibility Modelling, in: Engineering Geology for Society and Territory - Volume 2, pp. 201–204, Springer, Cham, https://doi.org/10.1007/978-3-319-09057-3_27, 2015.

Steger, S., Brenning, A., Bell, R., and Glade, T.: The Influence of Systematically Incomplete Shallow Landslide Inventories on Statistical Susceptibility Models and Suggestions for Improvements, Landslides, 14, 1767–1781, https://doi.org/10.1007/s10346-017-0820-0, 2017.

Steger, S., Schmaltz, E., and Glade, T.: The (f)Utility to Account for Pre-Failure Topography in Data-Driven Landslide Susceptibility Mod-
725 elling, Geomorphology, 354, 107 041, https://doi.org/10.1016/j.geomorph.2020.107041, 2020.

Talagrand, O., Vautard, R., and Strauss, B.: Evaluation of Probabilistic Prediction Systems, 1997.

Van Den Eeckhaut, M., Hervás, J., Jaedicke, C., Malet, J.-P., Montanarella, L., and Nadim, F.: Statistical Modelling of Europe-Wide Landslide Susceptibility Using Limited Landslide Inventory Data, Landslides, 9, 357–369, https://doi.org/10.1007/s10346-011-0299-z, 2012.

van Leeuwen, P. J.: Representation Errors and Retrievals in Linear and Nonlinear Data Assimilation, Quarterly Journal of the Royal Meteo-
730 rological Society, 141, 1612–1623, https://doi.org/10.1002/qj.2464, 2015.

Vanmaercke, M., Ardizzone, F., Rossi, M., and Guzzetti, F.: Exploring the Effects of Seismicity on Landslides and Catchment Sediment Yield: An Italian Case Study, Geomorphology, 278, 171–183, https://doi.org/10.1016/j.geomorph.2016.11.010, 2017.

Verdin, K.: Final Report High Resolution Topographic Analysis for GMAO's Catchment LSM, Tech. rep., Global Modeling and Assimilation Office, NASA/Goddard Space Flight Center, Greenbelt, MD 201771, 2013.

735 Verdin, K. L., Godt, J., Funk, C., Pedreros, D., Worstell, B., and Verdin, J.: Development of a Global Slope Dataset for Estimation of Landslide Occurrence Resulting from Earthquakes, Open-File Report 2007-1188, Colorado: U.S. Geological Survey, Reston, Virginia, 2007.

Whiteley, J. S., Chambers, J. E., Uhlemann, S., Wilkinson, P. B., and Kendall, J. M.: Geophysical Monitoring of Moisture-Induced Landslides: A Review, Reviews of Geophysics, 57, 106–145, https://doi.org/10.1029/2018RG000603, 2019.

740 Wilde, M., Günther, A., Reichenbach, P., Malet, J.-P., and Hervás, J.: Pan-European Landslide Susceptibility Mapping: ELSUS Version 2, Journal of Maps, 14, 97–104, https://doi.org/10.1080/17445647.2018.1432511, 2018.

Wilks, D. S.: Chapter 8 - Forecast Verification, in: International Geophysics, edited by Wilks, D. S., vol. 100 of *Statistical Methods in the Atmospheric Sciences*, pp. 301–394, Academic Press, https://doi.org/10.1016/B978-0-12-385022-5.00008-7, 2011.

745   Willmott, C. J. and Feddema, J. J.: A More Rational Climatic Moisture Index*, The Professional Geographer, 44, 84–88, https://doi.org/10.1111/j.0033-0124.1992.00084.x, 1992.

Zêzere, J. L., Pereira, S., Melo, R., Oliveira, S. C., and Garcia, R. A. C.: Mapping Landslide Susceptibility Using Data-Driven Methods, Science of The Total Environment, 589, 250–267, https://doi.org/10.1016/j.scitotenv.2017.02.188, 2017.

Zhu, J., Baise, L. G., and Thompson, E. M.: An Updated Geospatial Liquefaction Model for Global ApplicationAn Updated Geospatial Liquefaction Model for Global Application, Bulletin of the Seismological Society of America, 107, 1365–1385,

750   https://doi.org/10.1785/0120160198, 2017.

Zuur, A. F., ed.: Mixed Effects Models and Extensions in Ecology with R, Statistics for Biology and Health, Springer, New York, NY, 2009.